Three-Dimensional Modeling and Analysis of Magnetoplasmadynamic Acceleration

by

Brian J. Parma

A Thesis Presented in Partial Fulfillment
of the Requirements for the Degree
Master of Arts

Approved May 2011 by the
Graduate Supervisory Committee:

Pavlos G. Mikellides, Chair
Kyle Squires
Marcus Herrmann

ARIZONA STATE UNIVERSITY

August 2011

ABSTRACT

The Magnetoplasmadynamic (MPD) thruster is an electromagnetic thruster that produces a higher specific impulse than conventional chemical rockets and greater thrust densities than electrostatic thrusters, but the well-known operational limit—referred to as "onset"—imposes a severe limitation efficiency and lifetime. This phenomenon is associated with large fluctuations in operating voltage, high rates of electrode erosion, and three-dimensional instabilities in the plasma flow-field which cannot be adequately represented by two-dimensional, axisymmetric models.

Simulations of the Princeton Benchmark Thruster (PBT) were conducted using the three-dimensional version of the magnetohydrodynamic (MHD) code, MACH. Validation of the numerical model is partially achieved by comparison to equivalent simulations conducted using the well-established two-dimensional, axisymmetric version of MACH. Comparisons with available experimental data was subsequently performed to further validate the model and gain insights into the physical processes of MPD acceleration.

Thrust, plasma voltage, and plasma flow-field predictions were calculated for the PBT operating with applied currents in the range $6.5kA < J < 23.25kA$ and mass-flow rates of $1g/s$, $3g/s$, and $6g/s$. Comparisons of performance characteristics between the two versions of the code show excellent agreement, indicating that MACH3 can be expected to be as predictive as MACH2 has demonstrated over multiple applications to MPD thrusters. Predicted thrust for operating conditions within the range which exhibited no symptoms of the onset phenomenon experimentally also showed agreement between MACH3 and experiment well within the experimental uncertainty. At operating conditions beyond such values , however, there is a discrepancy—up to $\sim 20\%$—which implies that certain significant physical processes associated with onset are not currently being modeled. Such processes are also evident in the experimental total voltage data, as is evident by the characteristic "voltage hash", but not present in predicted plasma voltage. Additionally, analysis of the predicted plasma flow-field shows no breakdown in azimuthal symmetry, which is expected to be associated with onset. This implies that perhaps certain physical processes are modeled by neither MACH2 nor MACH3; the latter indicating that such phenomenon may not be inherently three dimensional and related to the plasma—as suggested by other efforts—but rather a consequence of electrode material processes which have not been incorporated into the current models.

ACKNOWLEDGMENTS

I would like to thank Dr. Pavlos Mikellides for his patience, guidance, and encouragement throughout this long process. Without the opportunities he provided I would not have come this far. I would also like to thank my colleagues and friends: Erik Henrikson and Heath Lorzel for their encouragement, advice, and assistance in completing my graduate program. Thanks also to my family who supported me throughout this long endeavor, always confident in my success. Lastly, I want to thank God for His love, my friends and family, and the opportunities he has placed before me.

TABLE OF CONTENTS

LIST OF TABLES

Table Page

LIST OF FIGURES

NOMENCLATURE

B = magnetic field, T

ξ = dimensionless current

m_a = mass of propellant atom, amu or kg

u_{cr} = critical ionization velocity, m/s

ϵ_i = ionization potential for i^{th} electron, eV

j = current density, A/m^2

μ_0 = permeability of free space, N/A^2

v = velocity, m/s

ρ = density, kg/m^3

P = pressure, Pa

σ_{ji}^d = elastic stress tensor

δ^{ji} = unit dyad

$T_{e(i)}$ = electron (ion) temperature, K or eV

$\epsilon_{e(i)}$ = electron (ion) specific internal energy, J

η = electrical resistivity, $\Omega - m$

$P_{e(i)}$ = electron (ion) thermanl pressure, Pa

n_e = electron number density, N/m^3

e = elementary charge of an electron, C

$\kappa_{e(i)}$ = electron (ion) thermal conductivity, $W/(m - K)$

Φ_{eR} = radiation coupling, W/m^3

$c_{v_{e(i)}}$ = electron (ion) specific heat, J/K

τ_{ei} = electron-ion equilibrium time, s

U_R = radiation energy density, J/m^3

G = shear modulus

χ_{ros} = rosseland mean opacity

μ = viscosity

γ = ratio of specific heats

E = electric field, V/m

CHAPTER 1

INTRODUCTION

Traditionally, space exploration has relied heavily on chemical propulsion technologies. Current and future long-range, or long-term, space missions, however, require more efficient utilization of propellant mass. From the rocket equation[1], this is equivalent to requiring a greater exhaust velocity from the propulsion system. The exhaust velocity of chemical rockets is limited by the amount of intrinsic energy available in chemical reactions, the unrecoverable energy deposition to internal modes, or "frozen flow" losses, and energy lost through heat transfer. Electric propulsion technologies are very attractive because they can provide solutions to these performance limiting problems inherent in chemical rockets. Electric propulsion is defined as[1]: "The acceleration of gases for propulsion by electrical heating and/or by electric and magnetic body forces". For electric thrusters the propulsive energy is deposited electrically, by an external source, instead of chemically, effectively removing the available energy limitation of chemical thrusters. This allows for a much greater range of exhaust velocities and equivalent space missions.

Electric propulsion concepts are classified based on their primary acceleration mechanism into electrothermal, electrostatic, and electromagnetic thrusters. Electrothermal devices electrically heat the propellant, usually by joule heating, and convert the enthalpy of the propellant into kinetic energy via expansion through a suitable nozzle. Such devices, however, are still limited by frozen flow and heat transfer losses. Electrostatic devices accelerate a pre-ionized propellant via direct application of electric body forces. These devices are not subject to the thermal limitations of chemical or electrothermal rockets, and can therefore achieve much higher exhaust velocities and greater efficiency. The necessity to pre-ionize the propellant, however, increases the complexity of the devices and associated propellant feed systems as well as limiting the practical mass-flow rate and, consequently, the thrust density. Additionally, beam neutralization is required to prevent excess charge from building up on the spacecraft and degrading thruster performance, which further increases complexity. Electromagnetic thrusters accelerate propellant via interaction of applied and induced electromagnetic fields with electric currents driven through the propellant. This allows more robust designs and greater thrust densities than electrostatic devices.

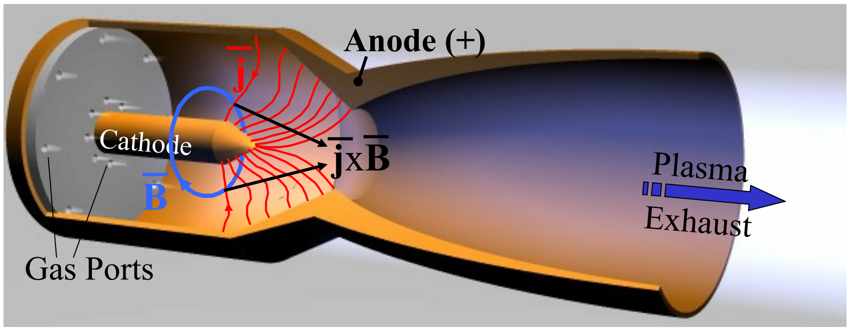

Figure 1. MPD Thruster diagram.

The Magnetoplasmadynamic (MPD) thruster, a simple schematic of which is shown by Figure 1, is one example of an electromagnetic thruster that can produce the desired elevated exhaust speeds. The MPD thruster is a steady-state electromagnetic accelerator that accelerates an ionized plasma through a channel and exhausts it to generate thrust. Specifically, A neutral gas is introduced into a cylindrical thrust chamber with an outer anode surrounding a central cathode[2]. An applied, radial arc current ionizes the gas and induces an azimuthal magnetic field. The interaction of the magnetic field and the current induces a Lorentz body force that accelerates the propellant axially and produces thrust.

Despite the increased simplicity of design and improved thrust densities, MPD thruster development and application has lagged compared to other electric rockets due to performance limitations that are not fully understood [3]. These limitations include high rates of electrode erosion and the “onset” phenomenon which limit the lifetime of the thrusters to orders of magnitude less than typical mission requirements. Onset is an observed phenomenon associated with increased erosion, large voltage fluctuations, and performance degradation at higher power level operation. There have been several theories put forth to try and explain onset[3, 4, 5, 6]. These theories include predictions that the onset phenomenon is due to an excessive back EMF force, due to electrothermal instability, due to magnetohydrodynamic instability, and due to anode starvation. Due to the complexity of the problem, however, the precise cause of onset is still not well understood.

Due to the complex, interdependent nature of the physics involved in MPD acceleration, any analytical approach would be impossible without simplifying assumptions that severely limit the applicability or accuracy of such an approach. Numerical investigation is, therefore, the next logical step toward a better understanding of the operation of an MPD thruster. To date, there has been a significant amount of progress in the numerical modeling of MPD thrusters[7, 8, 9, 10, 11, 12], which have yielded a better understanding of the operational modes, as well as suggesting potential performance improvements[7]. All of the previous work, however, has been performed with two-dimensional models assuming an axisymmetric flow. This has again limited the scope of investigations, and a fully three-dimensional numerical model is required to explore a phenomenon that is inherently asymmetrical. This work will describe a relatively new three-dimensional upgrade to a successfully utilized two-dimensional, axisymmetric code for the purpose of MPD modeling. This upgraded code has been previously validated[11] against analytical models and preceding numerical models, and in this effort it will also be validated by comparisons to available experimental data.

CHAPTER 2

BACKGROUND

There has been a great deal of periodic research on MPDs over the past three decades, which is detailed in literature[13, 14, 15]. This research has led to slow but steady improvements in MPD performance, but due to its performance and lifetime limitations, the MPD thruster has not received much attention in terms of real mission utilization. As mentioned above, these limitations are related to a phenomenon referred to as “onset”.

2.1. Previous Numerical Work

This section will outline some of the recent numerical research and development efforts focused on understand and improving the MPD thruster. Though, historically, much of the MPD research performed has been analytical and empirical, the continual technical advancements in computing is making numerical modeling increasingly viable. Consequently, there have been a number of recent research efforts focused on MPD thruster modeling.

The two-dimensional axisymmetric magnetohydrodynamic (MHD) code MACH2, described in more detail below, was originally designed to simulate collisional plasmas but has been successfully utilized to model the physics of MPD operation. MACH2 has been used to model the multi-megawatt MY-II MPD thruster[7], and this study led to a better understanding of the dominant energy modes of the thruster and suggested improved performance through proper nozzle expansion. The code has also been used to model the NASA

Lewis Research Center 100-kW applied field MPD [9]. This study showed that at the energy levels and geometry studied, the main acceleration mechanism was the conversion of thermal energy to axial thrust, and that the applied magnetic field did not interact with the low-density, low-conductivity argon plasma in the manner of a magnetic nozzle as expected.

Other numerical codes have also been independently developed and applied to the problem of modeling MPD operation. A group at Princeton has developed a code to include self-consistent treatment of flow and magnetic field equations, conservation formulation of equations, and a characteristics-splitting scheme [16, 17]. It was developed with the intention of more accurately capturing discontinuities such as shocks and MHD waves. The code has been subsequently validated and used to gain insights into the operation of the Princeton Benchmark Thruster, such as weak dependence of thrust on anode geometry, the predominantly electromagnetic nature of the thrust, and the importance of the near cathode region to plasma energy dissipation[18, 12].

Another independent code was developed to investigate plasma flows in self-field MPD thrusters. It was designed to solve the conservation equations describing a continuum-mechanical, turbulent axisymmetric argon plasma flow under the influence of an arc discharge in thermal and reaction non-equilibrium on adaptive, unstructured meshes [19]. This code was verified to accurately predict the thrust and arc shape of the modeled thruster. It was also used to suggest that the drop in density in front of the anode, due to the pinch effect, is the cause for the onset of performance degrading instabilities.

Substantial progress has been achieved over the past two decades in the numerical modeling of MPD acceleration. These efforts range from single-temperature, two-dimensional models on simple geometries [20, 21] to multi-temperature models [22, 23] and unstructured adaptive grids for various geometries with detailed ionization and transport models [24, 25]. With the exception of the three-dimensional upgrade of MACH2 to MACH3 [26, 11], however, numerical modeling of MPDs has been entirely two-dimensional.

2.2. Theories of Onset

The nature of MPD performance is such that both exit velocity and efficiency increase monotonically with the scaling parameter $J^2/\dot{m}$[1]. However, operating MPD thrusters at $J^2/\dot{m}$ beyond a limiting value—which scales with energy deposition to internal modes such as ionization—leads to a phenomenon commonly referred to as “onset”. This phenomenon is associated with terminal voltage oscillations, or “voltage hash”, anode spotting and increased rates of electrode erosion, non-azimuthal current distributions, and a non-azimuthal, unsteady plasma flow. Onset also has a dramatic impact on thruster performance. The efficiency of the MPD thruster operating beyond the onset limit is severely degraded, and the ablation of the anode places a limit on the lifetime of the thruster that is well below the necessary durations for useful missions.[27]

Over the years MPD research has led to many theories on the cause of onset, though the process is still not fully understood. Most of these theories relate to either current discharge or plasma instabilities [28, 4, 29, 5], anode mass starvation [30, 27], or thermodynamics [4, 3, 31, 29]. Instability theories suppose that when the operating current surpasses the critical current value, an instability in the plasma flow develops which breaks the axisymmetry and causes the symptoms observed in experiments. Anode mass starvation theories instead predict that as the acceleration increases the density drops until there are regions where there are insufficient charge carriers to transport the applied current. In this condition the thruster is starved for mass and current symmetry breaks down, causing the onset phenomenon. Other theories alternatively use thermodynamic conditions to analytically determine a theoretical limit to the operating conditions that is interpreted as onset.

The research in this area, however, has been predominantly analytical and empirical, and due to the complex, interdependent nature of the physics in the MPD thruster, the analytical models contain many simplifying assumptions that limit their ability to predict MPD thruster performance, especially beyond the onset limiting value.

The natural evolution of such approaches is to develop more accurate numerical models to study the performance and effects of operating beyond the onset limit. Although there has been ample numerical work in modeling MPD thruster operation, it has been mostly limited to well behaved modes of operation. The main reason for this is that until recently the capability of modeling MHD flows has been limited to two-dimensional, axisymmetric numerical codes. The onset phenomenon and its manifestations, however, are inherently three-dimensional, and therefore require a fully three-dimensional numerical code to study. The focus of this current study is present and verify an advanced, fully three-dimensional numerical code that can be used as a tool to study these problems.

2.2.1. Critical Current. Regardless of the cause, numerous MPD experiments have shown that the dimensionless current $\xi = J/J_{cr}$ scales various aspects of MPD behavior related to onset[32]. J_{cr} is a critical current related to ionization of the propellant. The physical interpretation of the critical current is generally as follows. As energy is deposited from the current into the plasma, most of it is deposited into useful acceleration of the plasma. This continues until the plasma reaches a point where additional energy deposited into the plasma goes toward ionization of the propellant (a phase change) instead of useful acceleration until it is fully ionized. The point where this occurs can be described by defining a nominal regime for MPD operation where an equipartition of energy (or power) sinks can be stated, in terms of power, as[32]

$$\frac{1}{2}Tu_{ex} = \dot{m}(\epsilon/M) \tag{2.1}$$

Or, in other words, the energy in the useful sink is equal to that required to ionize the plasma. ϵ is the first ionization potential of the propellant, and can be represented using the Alfven critical velocity, or critical ionization velocity, as

$$u_{cr} = \sqrt{\frac{2\epsilon}{m_a}} \tag{2.2}$$

From the preceeding two equations and the Maecker formula,

$$T = \frac{\mu_0 J^2}{4\pi}(\ln\frac{r_a}{r_c} + \delta) \tag{2.3}$$

which is described in section 6.1.1, the critical current can be estimated as

$$J_{cr} = \left[\frac{\dot{m}u_{cr}}{\frac{\mu_0}{4\pi}(\ln\frac{r_a}{r_c} + \delta)}\right] \tag{2.4}$$

The critical current can then be used to define the dimensionless current

$$\xi = J/J_{cr} \tag{2.5}$$

which is thought of as a similarity parameter in the sense that two thrusters operating at similar values of ξ are expected to exhibit similar characteristics[32]. This analysis works well for singly-ionized plasmas, but for operating conditions like those in this study, multiple ionization levels are observed. In this case, the critical current based on the first ionization level appears to be less "critical", and the value of critical current can be adjusted to account for extra ionization levels by including extra ionization potential levels in the Alfven critical velocity. These critical currents associated with higher ionization levels can be interpreted in the same fashion as the first critical current; specifically, they represent the currents at which we expect additional power to be deposited into ionization of the corresponding ionization level. Extending ξ to account for these additional ionization levels involves the minor modification to eq. 2.2:

$$u_{cr_j} = \sqrt{\frac{2\epsilon_j}{m_a}} \tag{2.6}$$

Substituting this modified critical velocity into eqs. 2.4 and 2.5 yields the updated expressions:

$$\begin{aligned} J_{cr_j} &= \left[\frac{\dot{m} u_{cr_j}}{\frac{\mu_0}{4\pi}(\ln\frac{r_a}{r_c} + \delta)}\right] && (2.7) \\ \xi_j &= J/J_{cr_j} && (2.8) \end{aligned}$$

CHAPTER 3

THEORY

The modeling of an MPD Thruster requires a complex, non-linear set of coupled equations that can describe a quasi-neutral plasma flow and it's interaction with electromagnetic body forces. Such a basic set constitutes the fundamental Magnetohydrodynamic (MHD) equations. MACH3 solves an augmented set of these equations, which are breifly described. This chapter concludes with derivations of the similarity parameters present in the equations and a description of the simplifications applied for this work.

3.1. Magnetohydrodynamic (MHD) Equations

The physics involved in the flow through an MPD channel include coupled aspects of compressible gasdynamics, ionized physics, electromagnetic field theory, and particle electrodynamics[1]. Any attempt to faithfully attend all of these processes, even numerically, would be a severely daunting task. Therefore, to obtain a useful model of the flow through an MPD thruster, we must make some simplifying assumptions about the nature of the flow and processes involved. One of the most common, and useful, approaches to this problem is the magnetohydrodynamic (MHD), or magnetogasdynamic, formulation. We assume the flow consists of a single, quasi-neutral fluid that behaves as a continuum in the presence of an electromagnetic field. The physical properties are then adequately described by a set of bulk thermodynamic properties and an equation of state that includes ionization. Similarly, the fluid's behavior can be described by a set of continuum conservation laws that include the additional body forces and energy exchanges associated with the interaction of the fluid with an electromagnetic field, Maxwell's equations, Ohm's law, and necessary constitutive and transport relations. With these considerations and the MHD approximation, $\nabla \times \vec{B} = \mu_0 \vec{j}$, the following set of equations can be derived[33].

Conservation of Mass:

$$\frac{\partial \rho}{\partial t} = -\nabla \cdot (\rho \vec{v}) \tag{3.1}$$

Conservation of Momentum:

$$\rho \frac{Dv^i}{Dt} = \nabla_j \left[-P\delta^{ji} + \frac{1}{\mu_0} \left(B^j B^i - \frac{1}{2} B^2 \delta^{ji} \right) + \sigma^d_{ji} \right] \tag{3.2}$$

Conservation of Energy for Electrons:

$$\rho \frac{D\varepsilon_e}{Dt} = -P_e \delta^{ji} \nabla_i v_j + \eta j^2 - \vec{j} \cdot \left(\frac{\nabla P_e}{e n_e} \right) + \nabla \cdot (\kappa_e \nabla T_e) - \Phi_{eR} - \rho c_{v_e} \frac{(T_e - T_i)}{\tau_{ei}} \tag{3.3}$$

Conservation of Energy for Ions:

$$\rho \frac{D\varepsilon_i}{Dt} = \left[-P_i \delta^{ji} + \sigma^d_{ji} \right] \nabla_i v_j + \nabla \cdot (\kappa_i \nabla T_i) + \rho c_{v_e} \frac{(T_e - T_i)}{\tau_{ei}} \tag{3.4}$$

Generalized Ohm's Law:

$$\vec{E} = \overleftrightarrow{\eta} \cdot \vec{j} - \vec{v} \times \vec{B} + \frac{1}{e n_e} \left(\vec{j} \times \vec{B} \right) \tag{3.5}$$

Generallized Ohm's Law can be combined with Faraday's Law and Ampere's Law to eliminate the electric field and current density. This produces the following magnetic induction equation.

Magnetic Induction:

$$\frac{\partial \vec{B}}{\partial t} = \nabla \times \vec{v} \times \vec{B} - \nabla \times \frac{\eta}{\mu_0} \nabla \times \vec{B} - \nabla \times \left[\frac{1}{e n_e \mu_0} \left(\nabla \times \vec{B} \right) \times \vec{B} + \frac{\nabla P_e}{e n_e} \right] \tag{3.6}$$

3.2. MACH Equations

The MACH codes solve an augmented version of the the preceeding set of dynamic, single-fluid, multi-temperature, resistive MHD equations. These equations are advanced in a time-split manner that implicitly treats diffusive processes. Implicit treatment of the computationally intense diffusion processes allows a relaxation of the time step size constraint without compromising stability. The following sections briefly describe MACH's treatment of the MHD equations, as much more detailed descriptions are available in literature[34, 35, 36].

3.2.1. Mass Conservation Equation. The conservation of mass equation is simply a statement of the balance between the rate of change of mass within a volume and the flux through the boundaries of that volume. MACH implicitly computes the Lagrangian time advance of the MHD quantities in a way that conserves mass, momentum, and magnetic flux[35].

3.2.2. Momentum Equation.

$$\rho\frac{Dv^i}{Dt} = \nabla_j\left[-\left(P+Q+\frac{1}{3}u_R\right)\delta^{ji}+\frac{1}{\mu_0}\left(B^jB^i-\frac{1}{2}B^2\delta^{ji}\right)+\sigma^d_{ji}\right] \tag{3.7}$$

MACH's momentum equation includes an artificial viscosity term Q and a radiation energy density term. The artificial viscosity is a pressure term that is a quadratic function of the divergence of the fluid velocity. The term is only present when the divergence of the fluid velocity is negative, and effectively smooths discontinuities to improve stability. This term can be controlled or zeroed depending on the problem. In addition, surface forces other than pressure are included in a bulk stress tensor σ^d_{ji}. This enables the modular use of any available or user created models. MACH2 currently contains Newtonian-fluid viscous (Navier-Stokes) and elastic-plastic stress models[8]:

$$\begin{aligned}\text{Viscous: } \sigma_{ji} &= \mu\left(v_{ij}+v_{ji}-\frac{2}{3}\delta^{ji}v_{kk}\right) &(3.8)\\ \text{Elastic: } \frac{\partial\sigma_{ji}}{\partial t} &= 2G\delta^{ji}-v^k\nabla_k\sigma^{ji} &(3.9)\end{aligned}$$

MACH3 has not yet been extended to include such stress models, but, for the MPD operating conditions studied, the effects of viscosity are assumed to be negligible based on large Reynolds numbers.

3.2.3. Energy Equations. The MACH codes can solve up to three energy equations: electron specific internal energy, ion specific internal energy, and radiation energy density. The electron and ion coupling is controlled by the user and can be set to assume equilibrium (single temperature) or non-equilibrium (two-temperature). MACH also has the ability to solve for the radiation energy density using the following equation:

$$\frac{Du_R}{Dt} = -\frac{4}{3}u_R\nabla \cdot \vec{v} + \nabla \cdot (\rho\chi_{ros}\nabla u_R) + \Phi_{eR} \tag{3.10}$$

MACH contains models for radiation emission, equilibrium radiation diffusion, and flux-limited radiation diffusion. These processes, however, have been assumed negligible and excluded from the studied simulations.

3.2.4. Equations of State and Transport Equations. In order to generate a solution, the set of MHD equations must be completed with an equation of state and transport equations. The equation of state and caloric equation of state prescribe the fluids pressure and specific internal energy based on number densities and temperatures[8]. The transport equations similarly define the transport coefficients, such as electrical diffusivity and thermal conductivity. These equations can be provided by either analytical models or tabular data. MACH can use a provided set of analytical models, including the ideal gas model and Grneisen model, or can be extended to include additional models.

The preferred method, though, is to use tabular models. These models are provided via the SESAME data tables generated by the T-4 group of the Theoretical Division at Los Alamos National Laboratory. These tables are packaged in SESAME equation of state data libraries and include thermodynamic properties and fractional ionization state based on Local Thermodynamic Equilibrium[8]. It is important to note that the tables do not take into account molecular disassociation, but this limitation does not affect this study, as only monotonic propellants are used. The libraries can also contain tables for photon transport, or opacity tables, and electron transport, but were not available for this work. Additionally, while not used here, independent tables can be generated to meet specific needs[37].

3.3. Non-Dimensionalization of the MHD Equations

The set of single-fluid MHD equations presented in section 12 can be further reduced by non-dimensionalization, or deriving the similarity parameters that scale their behavior. These similarity parameters can then be analyzed in the context of the physical MPD problem to determine the relative importance of present physical processes. The following set of non-dimensional parameters are considered:

$$\bar{x} = \vec{x}/L_c,\ \bar{v} = \vec{v}/U_c,\ \bar{t} = t/\left(L_c/U_c\right),\ \bar{\rho} = \rho/\rho_c,\ \bar{P} = P/P_c,$$

$$\bar{B} = \vec{B}/B_c,\ \bar{\eta} = \eta/\eta_c,\ \bar{\nabla} = L_c,\ \bar{n}_e = n_e/n_{e_C} = n_e/\left(Z\rho_c/m_i\right)$$

3.3.1. Momentum Equation. The momentum equation—or equation of motion—describes the evolution of the fluid's momentum in response to the surface and body forces acting on it. The surface forces include pressure and viscous forces. The body forces include electromagnetic forces, but neglect polarization and magnetization of the plasma as negligible[8]. Equation 3.2 includes the viscous forces in a more general stress tensor σ^d_{ji}, but it is more convenient for this formulation to explicitly express them as:

$$\bar{\sigma}^d_{ji} = \frac{L}{Re}\left(-\frac{2}{3}\bar{\mu}\left(\bar{\nabla}\cdot\bar{v}\right)\delta^{ji} + \bar{\mu}\bar{\nabla}\bar{v}\right) \tag{3.11}$$

Where we have additionally assumed that the fluid is homogeneous and isotropic, and that the Stoke's condition is satisfied.

Substituting the non-dimensional parameters into the momentum equation (eq. 3.2) yields:

$$\bar{\rho}\frac{D\bar{v}^i}{D\bar{t}} = \bar{\nabla}_j\left[-\frac{1}{\gamma M^2}\bar{P}\delta^{ji} + \frac{1}{M_m^2}\left(\bar{B}^j\bar{B}^i - \frac{1}{2}\bar{B}^2\delta^{ji}\right) + \frac{1}{Re}\bar{\sigma}^d_{ji}\right] \tag{3.12}$$

Which contains three similarity parameters. The first is the Mach number M, which is a measure of the compressibility effects. The second is the magnetic mach number M_m, which is a relative measure of inertial forces to magnetic forces. The third is the Reynolds number Re, which is a relative measure of the inertial forces to the viscous forces.

3.3.2. Magnetic Induction Equation. The magnetic induction equation describes the evolution of the magnetic field. It includes convection and diffusion of the magnetic field, the Hall effect, and electron pressure diffusion. Applying the non-dimensional parameters to the magnetic induction equation (eq. 3.6) yields:

$$\frac{\partial \bar{B}}{\partial \bar{t}} = \bar{\nabla} \times \bar{v} \times \bar{B} - \frac{1}{R_m} \bar{\nabla} \times \bar{\eta} \bar{\nabla} \times \bar{B} - \frac{\Omega}{R_m} \bar{\nabla} \times \left[\frac{1}{\bar{n}_e} \left(\bar{\nabla} \times \bar{B} \right) \times \bar{B} + \frac{P_{e_c}}{2P_{B_c}} \frac{\bar{\nabla} \bar{P}_e}{\bar{n}_e} \right] \tag{3.13}$$

This formulation introduces two additional similarity parameters. The first is the magnetic Reynolds number R_m, which is a relative measure of flow velocity to magnetic diffusion velocity or magnetic advection to magnetic diffusion. The second is the Hall parameter Ω, which is a relative measure of Hall currents to conduction currents. The final term in the equation is the gradient of the electron thermal pressure. When it is non-dimensionalized, it is preceeded by the ratio of thermal pressure to magnetic pressure, $\beta = \frac{P}{P_B}$, where the magnetic pressure is $P_B = \frac{B^2}{2\mu_0}$.

3.3.3. Similarity Parameter Analysis. The advantage of deriving similarity parameters is that they can provide insight into the relative importance of present physical phenomenon in the context of a specific problem, and in turn allow simplifications to be made to the physical model. From the pervious section, we have the following similarity parameters:

$$\begin{aligned}
\text{Mach Number: } M &= \sqrt{\frac{U_c^2 \rho_c}{\gamma P_c}} \\
\text{Magnetic Mach Number: } M_m &= \sqrt{\frac{\mu_o \rho_c U_c^2}{B_c^2}} \\
\text{Reynolds Number: } Re &= \frac{L_c U_c \rho_c}{\mu_c} \\
\text{Magnetic Reynolds Number: } Rm &= \frac{\mu_o L_c U_c}{\eta_c} \\
\text{Hall Parameter: } \Omega &= \frac{B_c}{\eta_c e n_{e_c}} \\
\text{Beta Parameter: } \beta &= \frac{P}{P_B} \qquad (3.14)
\end{aligned}$$

If we consider a typical operating condition for the high-power MPD thruster using Argon as a propellant, we can estimate the magnitudes of these parameters. The assumed values are shown in Table 1, and the values are representative of operation with a mass-flow rate of $6g/s$ and a current of $15kA$. Table 1 also shows the resulting similarity parameters calculated from these values. From these parameters we can make a few inferences for the simulations.

First we note that the Reynolds Number is much larger than one. This indicates that the viscous forces are insignificant when compared to the inertial forces, and we therefore exclude viscosity from our model. The Magnetic Reynolds number is also larger than one, though only by $\sim 60\%$. Consequently, we expect that both magnetic diffusion and magnetic convection contribute significatnly to the evolution of the flow.

Based on the average characteristic values the Hall parameter $\Omega \approx 0.2$. This indicates that the hall currents should be on average about 20% of the conduction currents. The hall currents are predominantly axial j_z currents and will have the effect of skewing the current distribution from purely radial to a distribution with current contours extending further downstream in the direction from the cathode to the anode. This effect is expected to be most pronounced in the region between electrodes, because in the plume region, though the density decreases, we expect the ionization level to increase as well as the electrical resistivity due to contributions from anomalous resistivity[23, 10]. Since we are primarily interested in integrated performance characteristics and the integration includes the total current distribution, incorporating distributions far downstream of the thruster exit, we do not expect such slight variations to substantially affect the integration for the total $\vec{j} \times \vec{B}$ force. Based on these arguments and the lack of a three-dimensional numerical routine for the Hall effect in literature, we have excluded it from the model. The ultimate justification of these assumptions, however, will be forthcoming after validation of the model by comparison to experimental data is performed.

Table 1. Similarity parameters for the MPD model.

Characteristic Values	Similarity Parameters
$\rho = 1 \cdot 10^{-4} \frac{kg}{m^3}$	$M \approx 47$
$P = 30Pa$	$M_m \approx 14$
$U = 7.5 \frac{km}{s}$	$R_e \approx 12000$
$B = 0.03T$	$R_m \approx 1.6$
$n = 10^{21} m^{-3}$	$\Omega \approx 0.16$
$\mu = 1 \cdot 10^{-5} \frac{kg}{m \cdot s}$	$\beta \approx 0.05$
$\eta = 500 \frac{m^2}{s} \cdot \mu_0$	

CHAPTER 4

COMPUTATIONAL MODELING

The simulation code used for this study is the Multi-block Arbitrary Coordinate Hydromagnetic (MACH) family of MHD codes. MACH is a general purpose, time-dependent MHD code for complex geometries[35]. It exists in a serial, two-dimensional axisymmetric version (MACH2) and a parallel, three-dimensional version (MACH3) that utilizes MPI to facilitate parallel processing. The code was designed to be relatively modular, so that its capabilities can be extended to include additional physical models which offers MACH the flexibility to solve a wide variety of non-ideal MHD problems.

The code has been used to gain understanding of a wide variety of high-density plasma configurations[35]. Additionally, the code has been subsequently upgraded over the years and applied to a diverse range of plasma problems, including those in electric propulsion. Specifically, the axisymmetric version of MACH has been instrumental to providing insights into the energy loss mechanisms[7] of self-field MPD thrusters, as well as acceleration processes[9] in applied-field MPD thrusters.

This chapter will breifly describe the basic concenpts of MACH that are required to construct a model. A more detailed description of MACH and how it works can be found in the manual[35].

4.1. Numerical Scheme

4.1.1. Geometry. The MHD equations are solved on a computational mesh that consists of arbitrarily shaped hexahedral cells. This mesh is a continuous image of a logical mesh composed of a patchwork of conjoined sub-meshes called blocks.[35] This modular design allows complex geometries to be decomposed into simpler subsections that can each be described by an individual block. Each block is solved as its own individual problem, with neighboring blocks used only as a source of boundary conditions.

Such a divide and conquer strategy is ideally suited to parallel processing, and MACH3 is designed to be run in a parallel processing environment where each processing node is responsible for one or more individual blocks. Because adjacent blocks are required to exchange boundary information, the Message Passing Interface (MPI) protocol is used to facilitate communication between nodes. This parallelization capability is necessary to perform any type of complex, three-dimensional simulations in a reasonable amount of time.

4.1.2. Boundary Conditions. The philosophy of MACH is such that the boundary conditions describe the limit of the conditions of the fluid as the boundary is approached[36]. The conditions at, and beyond, the boundary are therefore assumed to be known or simply related to conditions inside the boundary. MACH has the ability to model the most common boundary types for it's included set of physical models. The boundary conditions used in these simulations are described in section 5.2.2, but a more complete set of possible boundaries available in MACH is described in literature[36, 35].

As with most of their design, the MACH codes handle boundary conditions in a modular, generic fashion. Each block's computational mesh is padded with an extra set of "ghost" cells. This allows quantities on the interior mesh to be computed without any special treatment or modification of the difference equations at the boundaries. A wide range of desired boundary condition can therefore be applied by explicitly controlling the values that are placed in the ghost cells. In addition, ghost cells on internal boundaries are copied directly from the neighbor's mesh, making decomposition transparent to the numerical method.

4.2. MACH Upgrades

In order to successfully apply MACH3 to the specific problem of simulating the operation of a high-power MPD thruster, some upgrades to the code were necessary. Since MACH was provided in the form of its source code, modification is possible and even encouraged. The major modifications are described below and include porting to 64-bit, calculation and output of additional performance quantities, and the ability to input a custom, externally generated physical mesh. In addition, some minor bug fixes were required as well as re-implementing restart capability.

4.2.1. 64-bit Port. The locally available computational resources, while adequate for MACH2 simulations, make fully three-dimensional modeling of an MPD thruster in a reasonable amount of time infeasible. Fortunately, for this research, the processing power of ASU's High Performance Cluster, Saguaro, was made available. All of the nodes on Saguaro, however, run on 64-bit architecture and contain 64-bit implementations of the MPI libraries. Thus, in order to utilize the parallel processing power required to complete three-dimensional simulations, it was necessary to port MACH3 to 64-bit.

MACH uses the non-standard Cray Pointer FORTRAN extension to facilitate dynamic memory which would not be possible with standard FORTRAN 77. Due to the organizational structure of the code, however, most pointers are explicitly declared as type **integer**.On a 32-bit machine, both integers and memory pointers are the same size (32 bits). On a 64-bit machine, as on a 32-bit machine, an integer is 4 bytes (32 bits), but a memory pointer is 64 bits. To prevent truncation of memory pointers, and subsequent memory access errors, and preserve the organization of the code, all pointers are explicitly declared as type **integer*8**, or 64-bit integers. Similarly, all file pointers as well as pointers in C helper functions were re-declared in MACH3 and dependent libraries.

4.2.2. Custom Grid Loader. Both MACH codes include a fairly sophisticated set of mesh generation subroutines which are controllable through a set of user specified parameters. It is sometimes of interest, however, to explicitly specify a grid that may be difficult or impossible for the built-in generation subroutines to produce. For this reason the code was modified to include the ability to import an explicit grid specified in PLOT3D format. With this, a mesh can be created using an external program such as GridGen and imported into MACH for finer control over the computational mesh.

4.2.3. Performance Characteristic Calculations. MACH was upgraded to include calculation of additional performance quantities that are not normally computed for MHD plasma simulations but are of interest to propulsion scientists. These include integration of the propulsive thrust and plasma voltages.

4.2.3.1. *Thrust Calculation.* One of the main parameters used to measure MPD performance is Thrust. MACH, however, was designed for the simulation of plasmas and not specifically for propulsion, so it does not explicitly calculate the thrust. All the flow-field parameters required to compute the thrust, though, are simulated throughout the domain. An additional boundary condition was added to the code to identify boundaries as thrust producing. On these boundaries, the thrust is integrated by:

$$T_i = \int \left(p + \frac{B^2}{2\mu_0} \right) d\vec{A}_i + \rho(\vec{u} \cdot d\vec{A})\vec{u}_i \tag{4.1}$$

Where i is an axis and $\vec{dA}$ is calculated using:

$$\vec{dA} = \frac{1}{2}\sum_{j} \vec{r}_j \times \vec{r}_{j+1} \tag{4.2}$$

4.2.3.2. *Voltage Calculation.* In addition to the thrust calculation, a new subroutine for calculating the simulated plasma voltage was required. Due to the absence of available models for the sheath voltage drop at the electrodes, any simulated voltage will be lower than the experimental total voltage. Approximating the plasma voltage, though, does have some value as a relative measure of performance in terms of conversion of plasma-deposited power to exhaust kinetic power, i.e. thrust power. Furthermore, it can be used with experimental data to estimate the magnitude of voltage drop at the electrodes, as the distinction between plasma and electrode voltage drop often isn't available. In order to calculate the voltage across the plasma, we integrate Ohm's Law between the electrodes (eq. 4.3).

$$V = \int \vec{E} \cdot \vec{dl} = \int \left(\eta \vec{J} - \vec{u} \times \vec{B}\right) \cdot \vec{dl} \tag{4.3}$$

This integration is necessarily taken away from the backplate to avoid artificial influences from the boundary conditions. For the modeled thruster geometry (in Figure 2), the integration is taken at the gap between the extended section of the anode and the electrode.

CHAPTER 5

NUMERICAL MODELING

Simulations of the Princeton Benchmark Thruster (PBT), shown in Figure 2, operating with applied currents in the range $6.5kA < J < 23.25kA$ and mass-flow rates of $1g/s$, $3g/s$, and $6g/s$ are progressed to steady-state. Validation is partially achieved by comparison to equivalent simulations conducted using the well-established two-dimensional, axisymmetric version of MACH. Comparisons with available experimental data is subsequently performed to further validate the model and gain insights into the physical processes of MPD acceleration.

The three-dimensional simulations were performed on Arizona State University's Saguaro cluster described in section 5.3. Each simulation was executed on 37 processors for approximately 95 hours, requiring about 3500 CPU-hours per simulation. Convergence to steady-state was verified by examining the integrated quantities of thrust, voltage, and mass flux out of the domain. Figure 3 shows a typical plot of these quantities used to verify steady-state. Since only steady-state operation was sought for this study, the initial conditions were chosen only to maintain numerical stability during the large gradients that are seen during the transient period of the simulations.

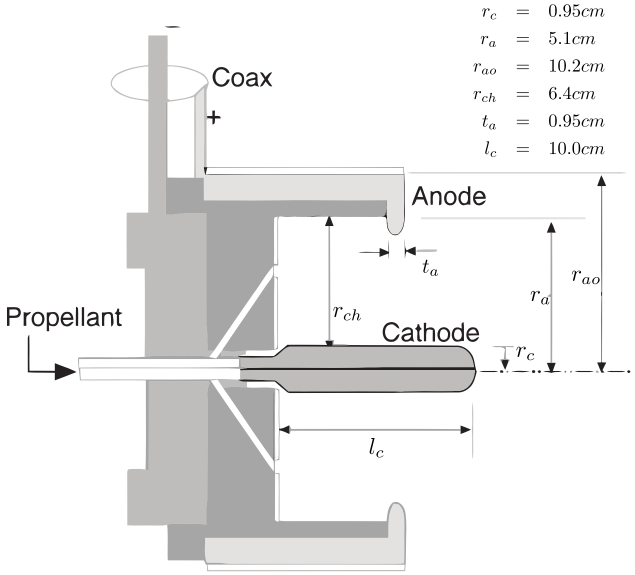

Figure 2. Princeton Benchmark Thruster (PBT) geometry.

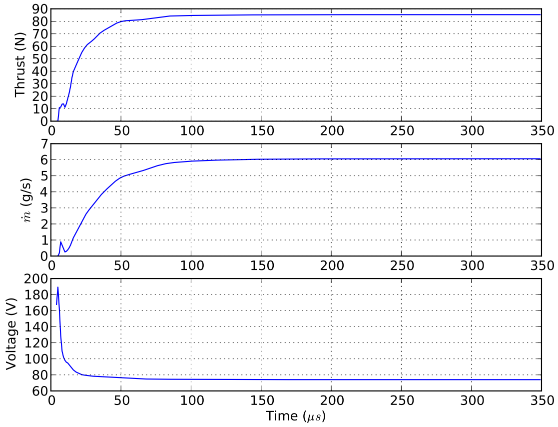

Figure 3. Integrated quantities verifying steady-state for MPD operation at $J = 22kA$ and $\dot{m} = 6g/s$.

5.1. Physical Setup

The experimental data used to validate these simulations is from the MPD Thruster performance database compiled by Choueri and Ziemer[38]. It includes thrust, voltage, and efficiency data of the coaxial, gas-fed, self-field Princeton Benchmark Thruster running in a quasi-steady pulsed mode of operation. The mass-flow rates included 0.5, 1, 3 and $6g/s$ runs using Ar, Xe, H_2, and D_2 as propellants. The propellant chosen for this study was Argon. The mass-flow rates available for Argon in the performance database were 1, 3 and $6g/s$, and all three were simulated. The operating current ranged from $6.5kA$ to $12.7kA$ for $1g/s$, $10.6kA$ to $20.9kA$ for $3g/s$, and $10.9kA$ to $23.25kA$ for $6g/s$.

The experiments were carried out in a quasi-steady mode utilizing a pulse forming network due to the low availability of steady high-power sources, especially in space. The pulse forming network, however, effectively simulates steady operation for up to several hundred μs and therefore can be used to describe steady-state operation[38]. To best capture such current variation, the numerical simulations model a constant current started by a short $5\mu s$ ramp up from zero to the desired operating current. Figure 4 shows typical current waveforms from the PBT experiments and MACH simulations.

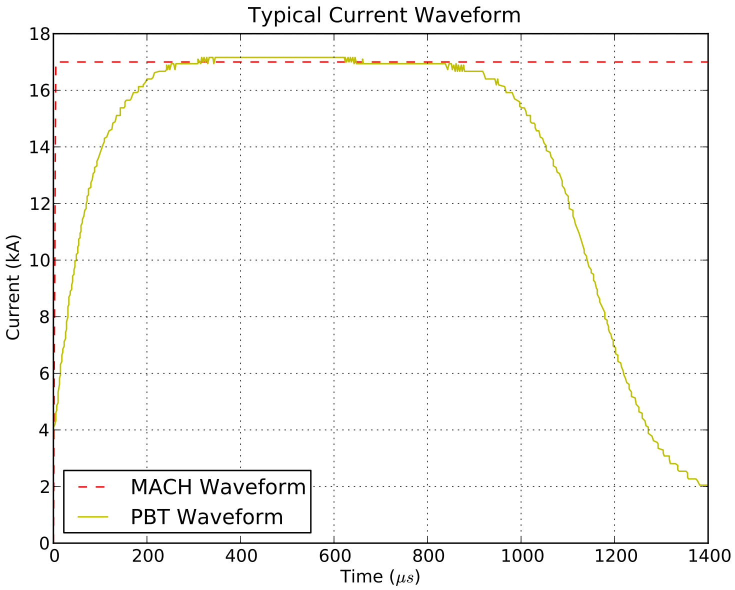

Figure 4. Typical current waveform at $J = 17kA$ from the PBT experiments and MACH simulations.

5.2. Geometry Setup

The thruster used to verify MACH3 is the Princeton Benchmark Thruster (PBT), shown in Figure 2 with dimensions. The PBT is a cylindrical thruster which is described in detail in other works[39, 38]. For the purpose of these simulations, a few simplifications are made to the model. The PBT injects its propellant through a choked multiple orifice which splits the flow such that 54% is injected at the cathode base and 46% is injected through a ring of 12 holes in the backplate located at 3.8 cm[12]. Since this would greatly increase the complexity of the grid and associated simulation time, a uniform mass injection is assumed across the backplate. This change has been shown not to severely affect the accuracy of axisymmetric simulations. The rounded tips of the anode lip and cathode tip are also flattened to simplify the complexity of the mesh and avoid numerical instabilities.

5.2.1. Computational Mesh. The computational domain for the PBT thruster includes the "thrust chamber", between the anode and cathode, and the "plume region", which contains the flow outside the thrust chamber and extends radially three times the anode radius and axially three times the cathode length. The dimensions of the computational domain ensure that all the currents are captured and that the normal gradients at the boundaries are small enough to justify free stream boundary conditions. The anode contains a lip that protrudes into the thrust chamber, and although this protrusion does not have a significant effect on thrust[12], it does act as a stagnation point that consequently affects the streamlines. Along with the choice of four blocks to span the azimuthal direction, the computational mesh in Figure 5, shown with a quarter cut away, is produced, containing 12 blocks for the thrust chamber, 24 blocks for the plume region, and one block for the center-line.

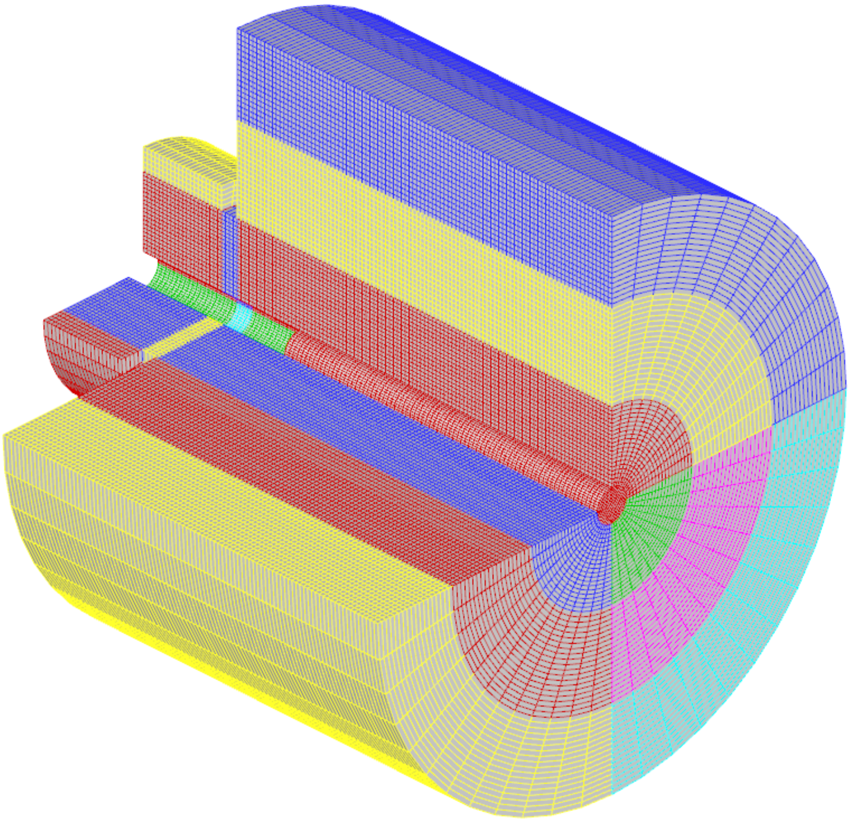

Figure 5. MACH3 Computational Mesh with 1/4 cut away

5.2.1.1. *Grid Resolution and Sensitivity Analysis.* The grid resolution used in all simulations was chosen such that accuracy of the implicit schemes is ensured while maintaining stability and preventing the amount of time for a simulation to reach steady-state from becoming prohibatively large. The code maintains stability of implicit methods by adjusting the timestep based on the fluid flow velocity, the Alven velocity ($V_A = B/\sqrt{\rho\mu_0}$), and a user-specified Courant number which was set to 0.8. MACH additionally restricts the timestep such that a user-specified, maximum amount of mass (which was set to 25%) can convect from a cell. With the chosen grid-cell dimension of $\Delta = 2.5mm$ and the code's restrictions, the simulations advanced at with typical timesteps in the range $5ns < t < 10ns$.

Diffusion of the magnetic field is modeled using implicit methods in MACH, and to ensure accuracy, we require the grid-cell dimension to be sized such that characteristic gradients are adequately captured. The characteristic dimension for magnetic diffusion gradients is the diffusion depth, $\delta = \sqrt{\eta\delta t}$. For typical timesteps, this characteristic length is on the order of $\delta \sim 5mm$, which implies gradient resolution on the order of $\delta/\Delta \sim 2$ for field diffusion.

The grid density can be further justified by conducting a grid sensitivity analysis. The analysis is performed by re-computing a simulated operating condition ($J = 12kA$ and $\dot{m} = 6g/s$) on progressively coarser grids. Four additional grids were used, with each one 20% coarser than the previous, and the simulations were allowed to converge to steady-state for comparisons of their performance characteristics. The results of the analysis, displayed in Figure 6, indicate that a 20% decrease in grid density has a negligible effect, with each examined value remaining within 2% of the baseline, confirming grid convergence. Decreasing the grid density further by 40% still maintains the integrated performance characteristics to within 5%, demonstrating low sensitivity to grid dimensions at the chosen resolution.

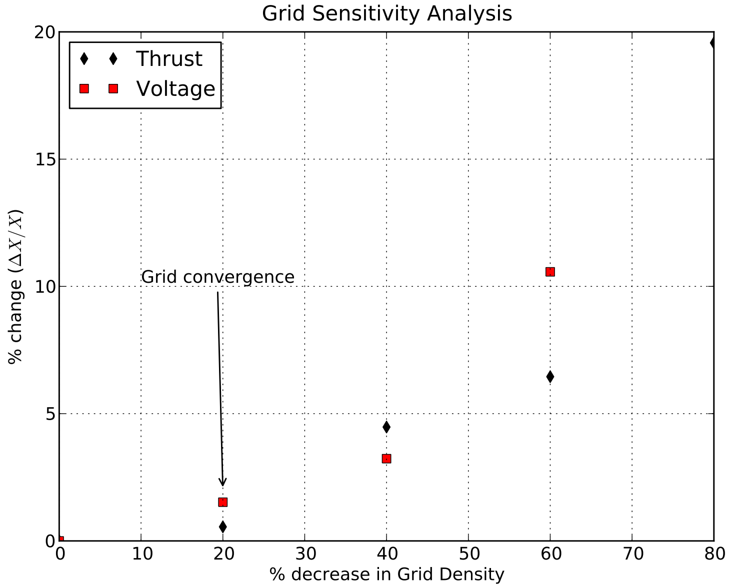

Figure 6. Performance characteristics for operation at $J = 12kA$ and $\dot{m} = 6g/s$ for different grid resolutions. Grid effectively converges at the resolution utilized for presented computations, displaying a discrepancy of less than 2%.

5.2.2. Boundary Conditions.

The set of boundary conditions applied to the model were chosen to reflect, as accurately as possible, the physical conditions that would exist for the MPD thruster in space or a vacuum chamber. The model's boundaries can be classified into four categories: the inlet, the insulating wall, the electrodes, and exhaust boundaries.

The inlet boundary contains the necessary information to inject a specified mass-flow rate into the problem domain. As previously mentioned, this boundary is applied to the entire backplate. The mass injection is achieved with specified density and velocity flows (eqs. 5.1 and 5.2)

$$\vec{v} = \vec{v_i} = v_\perp \tag{5.1}$$

$$\rho = \rho_i \tag{5.2}$$

where ρ and $\vec{v}$ are chosen such that $\dot{m}_i = \rho v_\perp A$ with $v_\perp = \sqrt{\gamma R T_i}$ and $A = \pi\left(r_{ch}^2 - r_c^2\right)$. The model injects the propellant as cold, $T_i = 300K$, neutral gas at sonic speed. It is possible, due to the difficulties with accurately modeling ionization breakdown[40], to inject the propellant as a pre-ionized gas. This has the effect of shifting the actual backplate a few millimeters behind that of the model's backplate[18]. This approach was not taken because it does not account for energy required to ionize, however small, or allow for partial ionization which is seen at higher mass-flow rates[12].

In addition to mass injection, a current boundary is applied to the backplate. The current boundary condition uses Ampere's Law to fill the ghost cells of the boundary with the resulting magnetic field(eq. 5.3). The magnetic field is then moved into the domain by the code's convective and diffusive subroutines.

$$\vec{B} = \frac{\mu_o \vec{j} \times \vec{r}}{4\pi r^3} \tag{5.3}$$

The insulating wall in the thrust chamber is similar to that of the inlet boundary with the exception of mass injection. Instead, a no-slip condition is applied to this boundary (eq. 5.4).

$$\vec{v} = 0 \tag{5.4}$$

Even though we have neglected viscosity in our equations due to large Reynolds numbers, the flow indeed does have a small boundary layer at physical boundaries. This boundary condition has the effect of creating a one cell thick boundary layer. The circuit-current boundary condition is also applied to the insulating wall to complete the "circuit" between the two electrodes.

The electrode boundaries cover the surfaces of both the anode and cathode. As with the insulating wall, a no-slip condition is applied to these boundaries. The magnetic boundary condition applied to these boundaries is that of an ideal conductor. For an ideal conductor, the normal component of the magnetic field and the tangential component of the electric field must be continuous, which implies[8]:

$$j_\theta = 0 \tag{5.5}$$

$$\hat{n} \cdot \bar{\nabla} \left(r B_\theta \right) = 0 \tag{5.6}$$

All the non-solid boundaries are considered exhaust boundaries. These boundaries are taken far enough away from the thruster that all the pertinent physical phenomenon and gradients are enclosed in the computational domain. As a result, Ampre's law states that the magnetic field, and thus magnetic pressure, at the exhaust boundaries are zero. The floor density, or minimum simulation density, was specified on the exhaust boundaries to simulate vacuum. This was chosen over a continuative boundary condition because the latter induced numerical instabilities which lead to incorrect results.

5.3. Computational Resources

The three-dimensional simulations were performed at Arizona State University using the Saguaro cluster, the centerpiece of ASU's High Performance Computing Initiative. The Saguaro cluster is composed of 220 dual quad-core Intel Xeon EM64T nodes. Each node has 16 gigabytes of memory and is linked via Cisco Infiniband high speed interconnects and gigabit copper. Saguaro has an additional 185 nodes with Intel Xeon MP 64bit processors for serial jobs, giving it a total of almost 2200 processor cores, 4000GB of memory, and 5TB of storage space.

CHAPTER 6

RESULTS

The following sections present the simulation results. Unless otherwise specified, comparisons with physical data are made against the Princeton Benchmark Thruster (PBT). Some simple analytical models are also used for comparison where appropriate. First, the general performance characteristics of the models are presented, then analysis proceeds based on three-dimensional distributions of the flowfield properties.

6.1. Performance Characteristics

6.1.1. Thrust Comparison. The thrust for the MACH simulations was calculated using eq. 4.1. From the flow-field and integrating the pressure over the exhaust boundaries, it was clear that the dominant component of the thrust was the momentum flux, and that the static and magnetic pressures were negligible. This was expected as the computational domain was chosen to be large enough to totally include the current distribution, and the magnetic field at the boundaries should be zero. In addition to experimental data and two-dimensional simulations, the Maecker formula is included for comparison.

The Maecker formula is a very basic formula that is derived by integrating the $\vec{j} \times \vec{B}$ forces for a cylindrical MPD thruster assuming azimuthal uniformity, purely radial current except the cathode tip, and a simplified axial distribution[41]. The model can be expressed as

$$T = bJ^2 \tag{6.1}$$

The coefficient b is a parameter based on the geometry of the thruster and current distribution over the cathode tip. It is generally approximated as

$$b = \frac{\mu_0}{4\pi} \ln\left(\frac{r_a}{r_c} + \delta\right) \tag{6.2}$$

where r_a and r_c are the radii of the anode and cathode, and δ is the cathode tip parameter and depends on the current distribution. This parameter can also be approximated from data by plotting T/J^2 as a function of current[2]. At high-power operation, there is an approximately constant region that can be described by the Maecker formula. The model is adequately accurrate at high $J^2/\dot{m}$ levels, but does not capture the magnitudes or trends at low power levels. The operating conditions of these simulations, though, are high power, and the flow is expected to be fully ionized close to the inlet[18]. For this reason, only the simple Maecker model is considered here.

The primary shortcoming of the Maecker formula is that, while δ can be determined by a least-squares fit to the data to make Maecker fit very well, it is not known before aquiring data. This makes Maecker relatively ineffective as a predictive model. δ is a parameter that represents the additional thrust component imparted to the thruster due to the unique current distribution over the cathode tip and depends on thruster geometry as well as flowfield characteristics[1]. This makes it difficult to approximate theoretically, and therefore it is generally simply set to $\delta = 0$ for no current attachment or $\delta = 3/4$ for full current attachment. For the chosen thruster and operating conditions $\delta = 3/4$ greatly over-estimates the thrust, so $\delta = 0$ is used for the following plots.

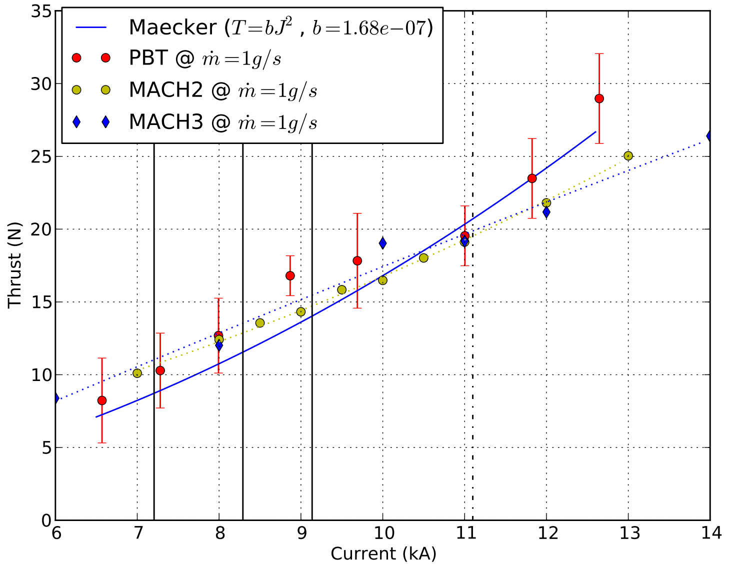

Figure 7. Experimental, MACH2, MACH3, and Maecker Thrust vs. Current for a mass-flow rate of $1g/s$. $\xi = 1$, $\xi = 2$ and $\xi = 3$ are shown as vertical black lines at $7.21kA$, $8.291kA$ and $9.1368kA$, and the point of 10% voltage hash shown as verticle dashed line at $11.1kA$

Figure 7 contains the plots of Thrust vs. Current for a mass-flow rate of $1g/s$. The plot compares MACH3 results to MACH2, the Maecker formula, and experimental data. Additionally, three vertical lines are included to mark the condition where $\xi = 1$ $(J = 7.21kA)$,$\xi = 2$ $(J = 14.4kA)$ and where the experimental voltage hash, or uncertainty, exceeds 10% of the average value ($J = 11.1kA$). The comparisons in the figure show reasonable agreement between the numerical simulations (both in two-dimensional axisymmetric and three-dimensions) and experimental data for $1g/s$. At lower current levels the predicted thrust values are well within experimental uncertainty. As operating current increases the discrepancy also increases to a range of $7 - 15\%$. The fidelity of the recently developed three-dimensional code, MACH3, is further increased since predicted thrust agrees extremely well with the well-established and repeatedly validated[7] two-dimensional version of the code, MACH2, for a wide range of MPD geometries and operating conditions. Such agreement, however, also indicates that three-dimensional physics do not significantly alter integrated performance parameters such as thrust. This notion is further explored in later sections. The Maecker formula comparison identifies the approximately parabolic trend as expected for a thruster operating in high power mode, wherein the electromagnetic thrust contribution dominates over other modes of kinetic energy conversion such as enthalpy conversion.

Figure 8 depicts thrust comparisons for operation at a mass-flow rate of $3g/s$. Similar trends are identified wherein simulated thrust values agree well with experiment for lower current operation. As the current increases, the discrepancy also increases by MACH3 and MACH2 predictions. They underpredict experimental thrust values by a maximum of 20%. Approximately the

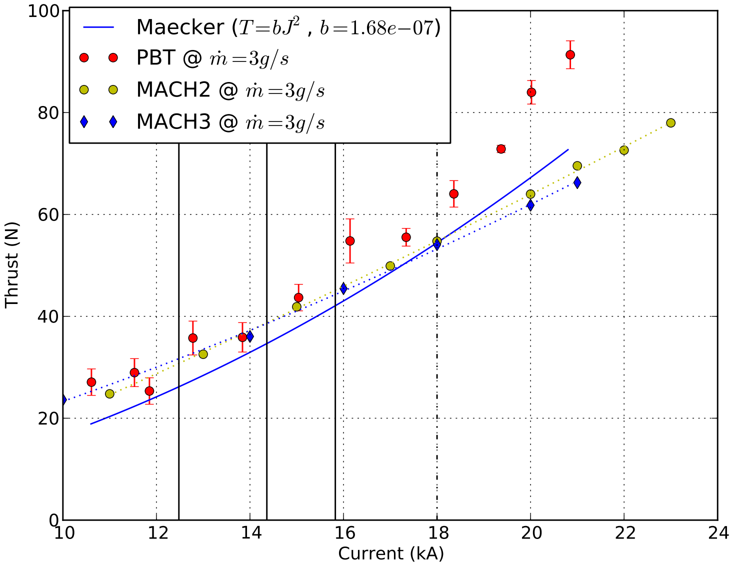

Figure 8. Experimental, MACH2, MACH3, and Maecker Thrust vs. Current for a mass-flow rate of $3g/s$. $\xi = 1$, $\xi = 2$ and $\xi = 3$ are shown as vertical black lines at $12.5kA$, $14.361kA$ and $15.825kA$, and the point of 10% voltage hash shown as verticle dashed line at $18kA$

same insights emerge from comparisons at thruster operation of $6g/s$ depicted by Figure 9.

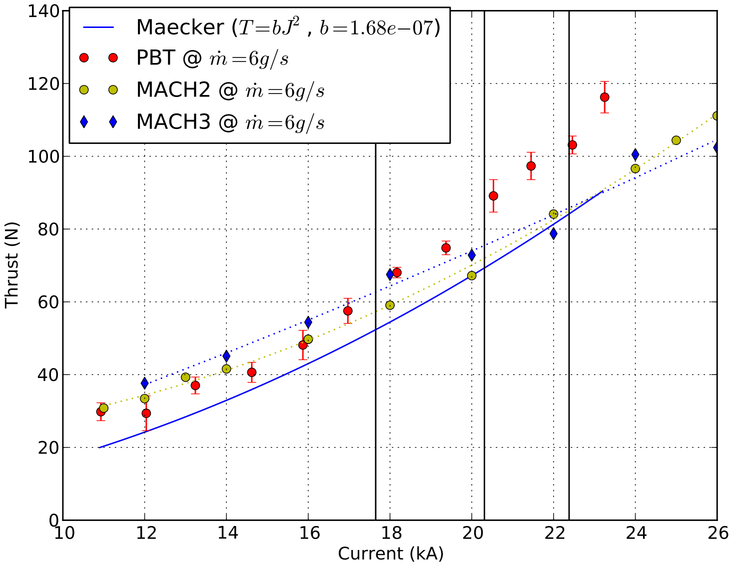

Figure 9. Experimental, MACH2, MACH3, and Maecker Thrust vs. Current for a mass-flow rate of $6g/s$. $\xi = 1$, $\xi = 2$ and $\xi = 3$ are shown as vertical black lines at $17.65kA$, $20.309kA$ and $22.380kA$. Voltage hash only reached 8% for the range of data included.

Validation of the newly-developed three-dimensional MHD code, MACH3, has been partially accomplished by thrust comparisons to experimental data and the well-established, repeatedly validated two-dimensional, axisymmetric version of the code, MACH2. Specifically, the predicted thrust values from the two numerical models are in excellent agreement, indicating that MACH3 can be expected to be as predictive as MACH2 has demonstrated over multiple applications to MPD thrusters. Agreement to experimentally measured thrust for lower to medium-level current operation was also shown to be well within empirical uncertainty for mass-flow operation within $1g/s < \dot{m} < 6g/s$. A more substantial discrepancy between experiment and simulation was observed at current operation beyond such values at which “onset” related phenomenon are present in experiment, e.g. significant voltage fluctuations. This implies that perhaps certain physical processes that may be associated with such fluctuations are modeled by neither MACH2 nor MACH3; the latter indicating that such phenomenon may not be inherently three dimensional and related to the plasma—as suggested by other efforts—but rather a consequence of electrode material processes which have not been incorporated into the current models.

6.1.2. Voltage Comparison. Plasma voltage from several simulations were calculated using eq. 4.3, and the integration was taken at the gap between the extended section of the anode and the electrode. Figures 10, 11, and 12 depict such voltage comparisons for $1g/s$, $3g/s$, and $6g/s$, respectively, to experimental measurements of total voltage which includes two contributions; voltage drop across the plasma (plasma voltage) and voltage drop across thin sheath electrode regions which are necessary such that charge plasma neutrality is maintained over a positive column. These voltage drops are referred to as fall voltages and are not modeled by the MACH codes as they require sub-grid physical models of Debye length scales.

The plasma voltage calculations from the simulations under-predict the experimental total voltage as much as 80% in some cases. This is expected[8] as neither MACH code is yet equipped with a model for fall voltage drop at the electrodes. Hence, the difference between plasma voltage and the experimental total voltage can be interpreted as an approximation of electrode fall voltage[8] which in turn is an indication of the relative power deposited to the sheath region. A self-consistent model that includes both plasma and fall voltage calculations would be preferrable, however previous work and validation by comparisons to experimental plasma voltage data for a single thruster has shown very good agreement using the MACH2 code[9].

Along with under-predicting, the voltage plots don't capture the non-linear

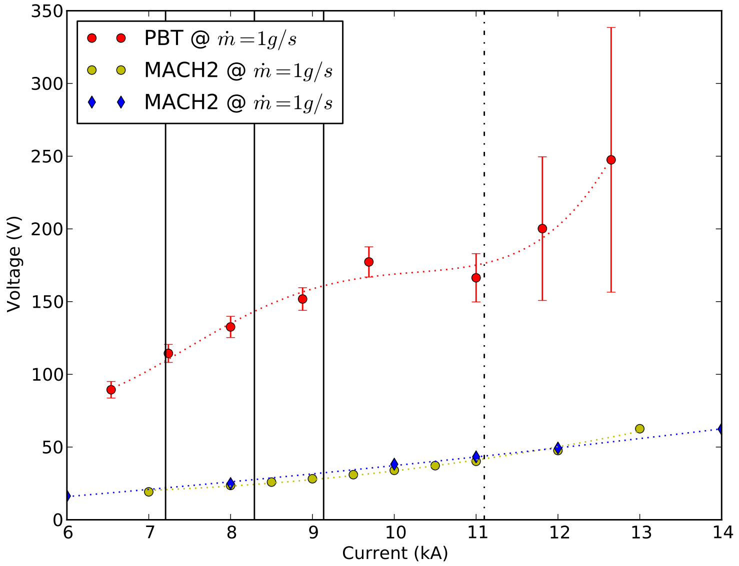

Figure 10. Experimental total voltage (plasma voltage + fall voltage) and MACH2, MACH3 predicted plasma voltage vs. Current for a mass-flow rate of $1g/s$. $\xi = 1$, $\xi = 2$ and $\xi = 3$ are shown as vertical black lines at $7.21kA$, $8.291kA$ and $9.1368kA$, and the point of 10% voltage hash shown as verticle dashed line at $11.1kA$

rise in voltage associated with the onset phenomenon. Also, because the model treats the electrodes as simple, ideal conductors, the simulations don't exhibit the characteristic voltage hash that accompanies onset experimentally. The comparisons seem to support the hypothesis that these effects are primarily associated with an electrode, material-related phenomenon such as anode spotting[8, 27], which coincides with the breakdown of azimuthal symmetry of the flow-field.

Anode spotting involves 'hot spots', or spots where the flow of current between the electrodes concentrates instead of distributing uniformly and may

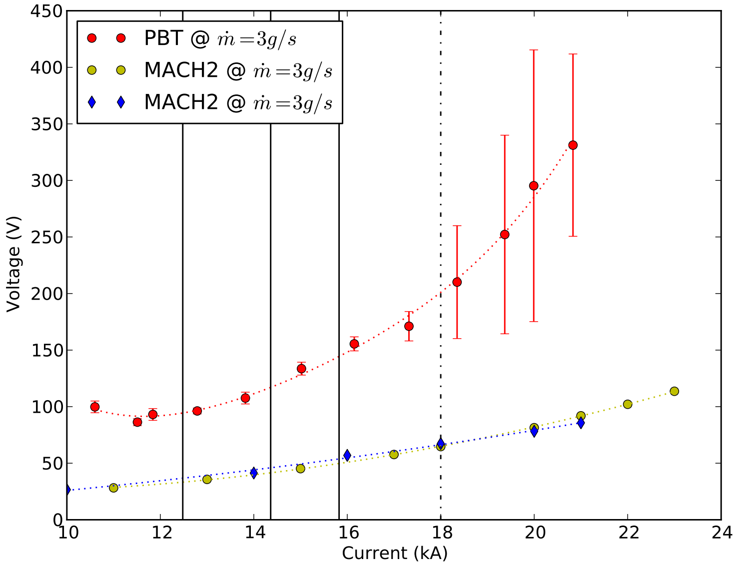

Figure 11. Experimental total voltage (plasma voltage + fall voltage) and MACH2, MACH3 predicted plasma voltage vs. Current for a mass-flow rate of $3g/s$. $\xi = 1$, $\xi = 2$ and $\xi = 3$ are shown as vertical black lines at $12.5kA$, $14.361kA$ and $15.825kA$, and the point of 10% voltage hash shown as verticle dashed line at $18kA$

be initiated by electrode material imperfections and roughness. These spots of high current, and resulting high temperature, deteriorate the electrode, causing pits and ablation of extra mass into the thrust chamber. The current model using MACH does not include the possibility for such surface variations, even though it is within its capability since the three-dimensional version can combine azimuthal boundary variation coupled with several ablation models already included in MACH. The electrodes are simply region boundaries with specified uniform boundary conditions. As a result, no fluctuations in mass-flow rate or voltage hash can be predicted. Another interesting result is

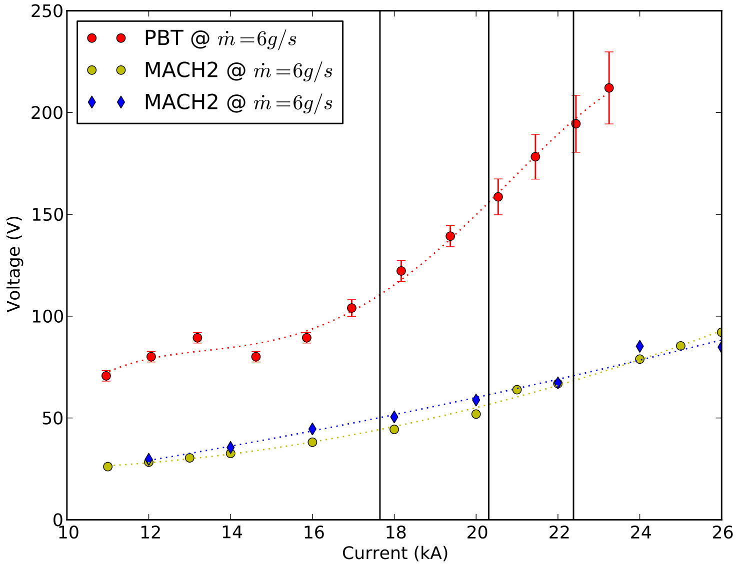

Figure 12. Experimental total voltage (plasma voltage + fall voltage) and MACH2, MACH3 predicted plasma voltage vs. Current for a mass-flow rate of $6g/s$. $\xi = 1$, $\xi = 2$ and $\xi = 3$ are shown as vertical black lines at $17.65kA$, $20.309kA$ and $22.380kA$. Voltage hash only reached 8% for the range of data included.

that the three-dimensional flow-field of the simulation results show azimuthal symmetry, even past the point of onset. This further supports that the anode spotting and breakdown of symmetry may be due to imperfections in the electrodes, which MACH does not model, instead of a plasma instability or thermodynamic causes[4, 3].

Assuming the difference in calculated plasma voltage and experimental total voltage is equal to the fall voltage, we can estimate how much power is deposited into the electrodes. Figure 13 shows the estimated power deposited to fall voltage vs. current for each mass-flow rate.

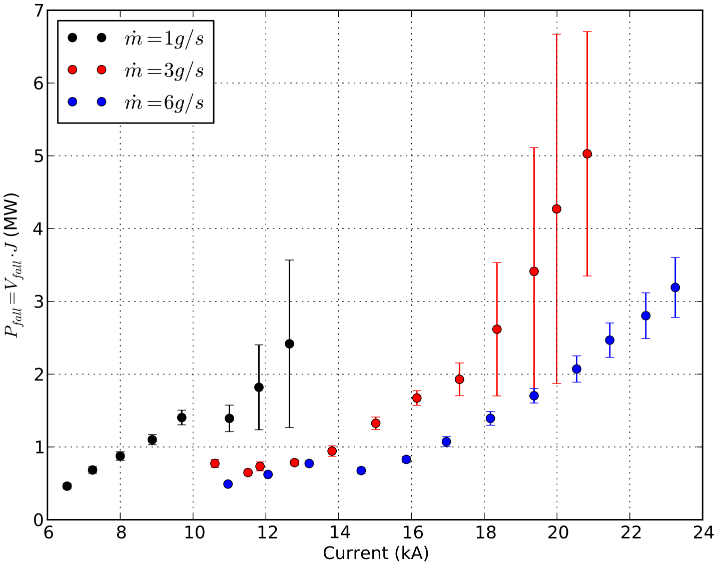

Figure 13. Power deposited into electrode sheaths ($P = J \cdot V_{fall}$) based on estimating fall voltage as the difference between experimental voltage and calculated plasma voltage.

The total power input into the thruster is the product of the total voltage and operating current, which are available by the experimental data. Comparing the experimental input power to the fall power shows that between 60% and 80% of the input power is being deposited to the electrode sheaths.

The input power that does get deposited into the plasma is divided further into useful acceleration and deposition to internal modes. The power deposited into internal modes is refered to as 'frozen flow' losses, and further impairs efficiency. The relative fractions can be estimated by calculating the kinetic power (thrust power) using eq. 6.3. The remaining power is the frozen flow power.

$$P_K = \frac{T^2}{2\dot{m}} \tag{6.3}$$

Using the calculated kinetic power and fall power above, the frozen flow power can be determined. The simulation thrust is used to calculate the kinetic power, because the simulation voltage is used to determine the total plasma power. This voltage doesn't include the fluctuations due to onset, and if used with the experimental thrust that is effected by onset, the diverging thrust in the onset region of the plots would result in a non-physical spike in efficiency. Figures 14, 15, and 16 shows the resulting power budgets for $\dot{m} = 1g/s$, $\dot{m} = 3g/s$, and $\dot{m} = 6g/s$.

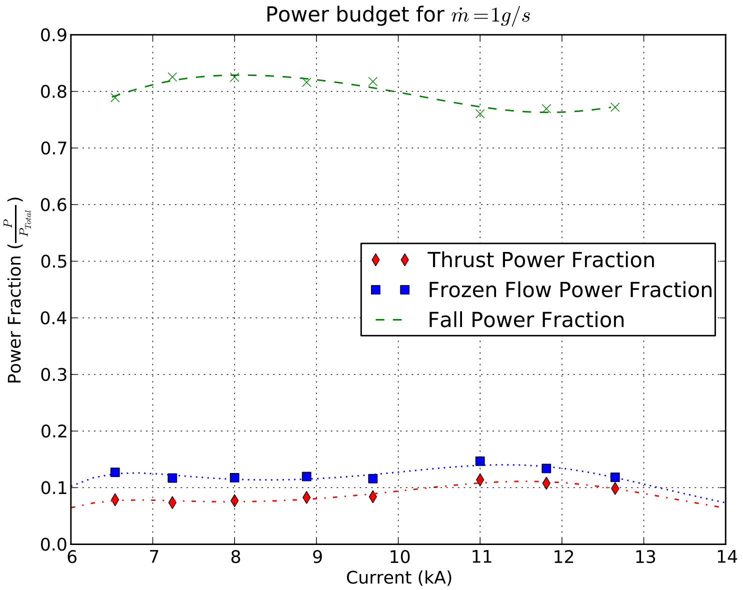

Figure 14. Power budget for $\dot{m} = 1g/s$ using voltage and thrust calculated by MACH3

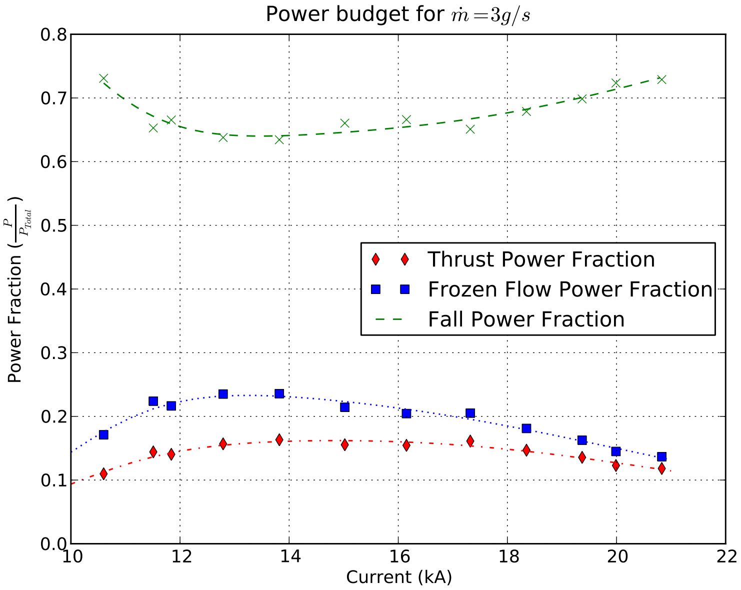

Figure 15. Power budget for $\dot{m} = 3g/s$ using voltage and thrust calculated by MACH3

From the figures, it is clear that the majority of input power is deposited into the electrode sheaths. The power deposited into the plasma is divided more evenly between the two major power sinks, with $40\% - -50\%$ of the plasma power going to useful thrust and $50\% - 60\%$ of the plasma power deposited into internal modes, e.g. heating and ionization.

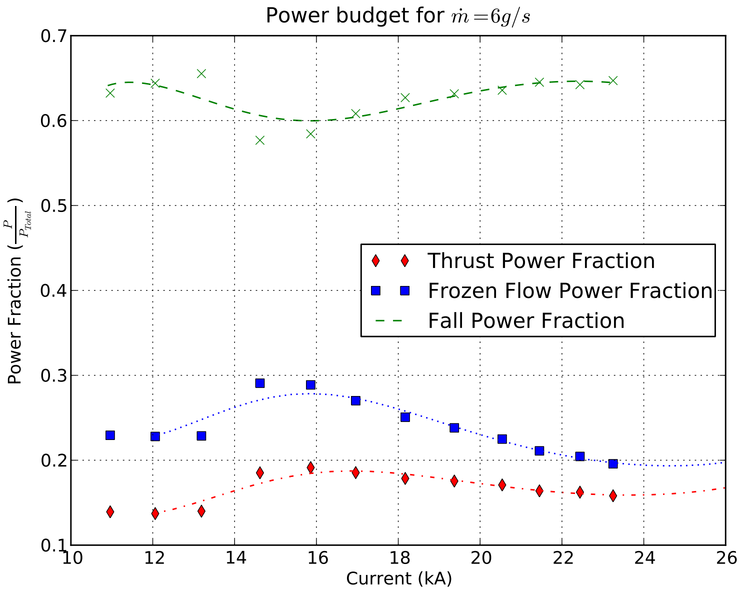

Figure 16. Power budget for $\dot{m} = 6g/s$ using voltage and thrust calculated by MACH3

6.2. Flow-field Analysis

The experimental data did not include any flow-field distributions, and therefore it is not possible to validate that aspect of the simulations. On the other hand, the three-dimensional nature of the flowfield properties can provide additional insights not available by experiments, especially when compared to the two-dimensional model. Analysis and interrogation of the flowfield property distributions is carried out for the representative operating conditions of $J = 12kA$ at $\dot{m} = 1g/s$ and $\dot{m} = 6g/s$ for minimum and maximum mass flow rates, and $J = 24kA$ at $\dot{m} = 6g/s$ which represents the higher power range. Three-dimensional distributions of density, current, temperature and average degree of ionization are investigated and compared to their two-dimensional, axisymmetric counterparts generated by MACH2.

Each MACH3 figure consists of two slices perpendicular to the flow axis, one between the electrodes and one in the exhaust plume, a slice along the flow axis, and a solid contour plot with a quarter cut out. The overarching feature that is clearly evident after a brief assessment of all property distributions shown is that MACH3 suggests that the flowfield is mainly azimuthally symmetric even for simulations at the high current level beyond which the experiments have shown the fluctuations and rapid voltage increases associated with onset. As mentioned above, such phenomenon are expected to breakdown azimuthal symmetry, as the depleted current carriers would tend to form arcs that are concentrated in smaller regions at the electrodes as opposed to being uniformly diffused. This tends to support previous inferences that onset phenomenon and the associated azimuthal asymmetry may be initiated by electrode surface imperfections, which tend to provide the preferred current paths, as opposed to plasma inherent processes such as micro-instabilities and/or thermo-chemistry.

A figure consisting of the corresponding MACH2 simulation follows each set of MACH3 plots. For most of the plots the contours match very well considering they are generated by two separate codes with different grid densities. The main difference between MACH3 and MACH2 in most of the plots occurs in the section of the plume that extends past the anode. This difference, though, is completely numerical. For the MACH2 simulations, the exhaust boundaries are generally set to continuative, or zero-gradient[7], with the assumption that the gradients at those surfaces are small enough to be considered negligible. In MACH3, however, a numerical instability prevented the use of continuative boundary conditions on these boundaries, and instead, the boundary conditions were set to simulate vacuum. This difference in boundary conditions allows the gradients tangent to the boundaries to more easily propagate along those boundaries in MACH2 than in MACH3, leading to different steady-state flow-fields in the region where the anode boundary joins the exhaust boundary. Fortunately, this is a very low density region, and it is clear from the integrated quantities that this difference has a negligible effect on the performance characteristics, i.e. thrust and voltage.

The numerical nature of this difference is confirmed by re-simulating the two-dimensional simulation for the most effected case ($J = 12kA$ and $\dot{m} = 1g/s$). The resulting current contours are shown in Figure 41 (in section A of the APPENDIX) and show much better agreement to the three-dimensional version in Figure 29. The performance quantities are also computed for this simulation and show differences in both thrust and voltage of less than 3% when compared with the three-dimensional version.

Figures 17 and 18 show the density contours for the $J = 12kA$ at $\dot{m} = 1g/s$ case. The mass flows through the thrust chamber and expands in the plume region. There is also some mass pinched to the center-line due to the Lorentz ($\vec{j} \times \vec{B}$) force and the curvature of the current lines as they connect to the cathode tip. While similar, MACH2 predicts density distributions that are pushed further downstream than in MACH3. The flow in MACH experiences a more severe pinching force due to the difference in current contours and their resulting Lorentz forces. As previously mentioned, this is caused by the difference in boundary conditions between MACH2 and MACH3, but has negligible impact on performance characteristics.

Figures 19 and 20 show the mass flow rate for the $J = 12kA$ at $\dot{m} = 6g/s$ case, and it is similar to the $\dot{m} = 1g/s$ case with the exception of higher

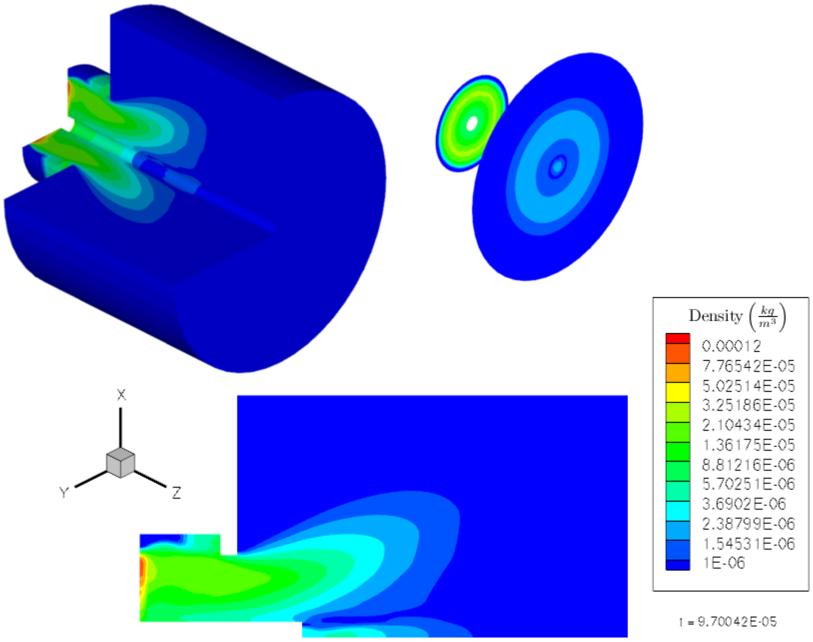

Figure 17. MACH3 density contours at $J = 12kA$ and $\dot{m} = 1g/s$

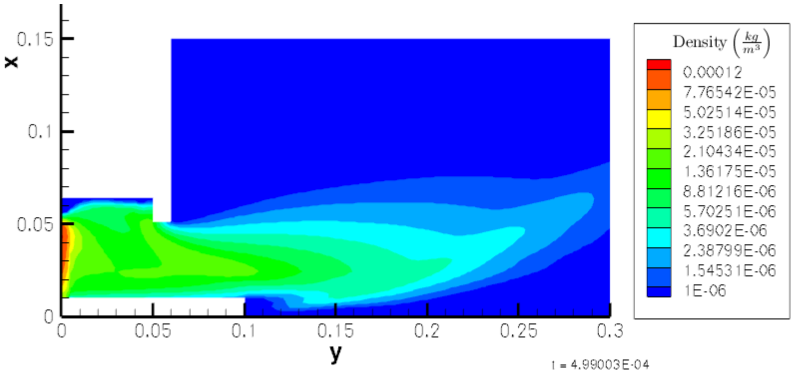

Figure 18. MACH2 density contours at $J = 12kA$ and $\dot{m} = 1g/s$

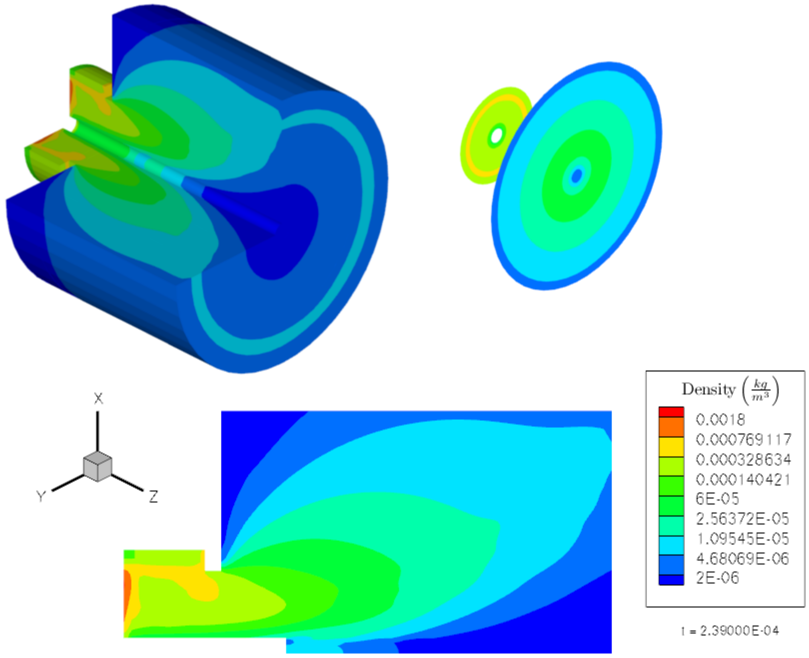

Figure 19. MACH3 density contours at $J = 12kA$ and $\dot{m} = 6g/s$

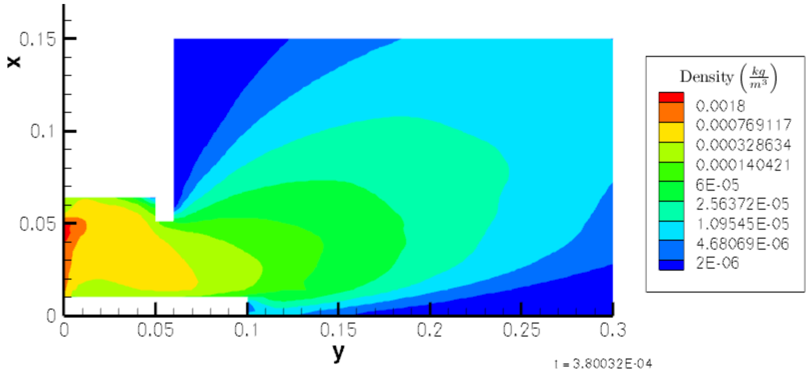

Figure 20. MACH2 density contours at $J = 12kA$ and $\dot{m} = 6g/s$

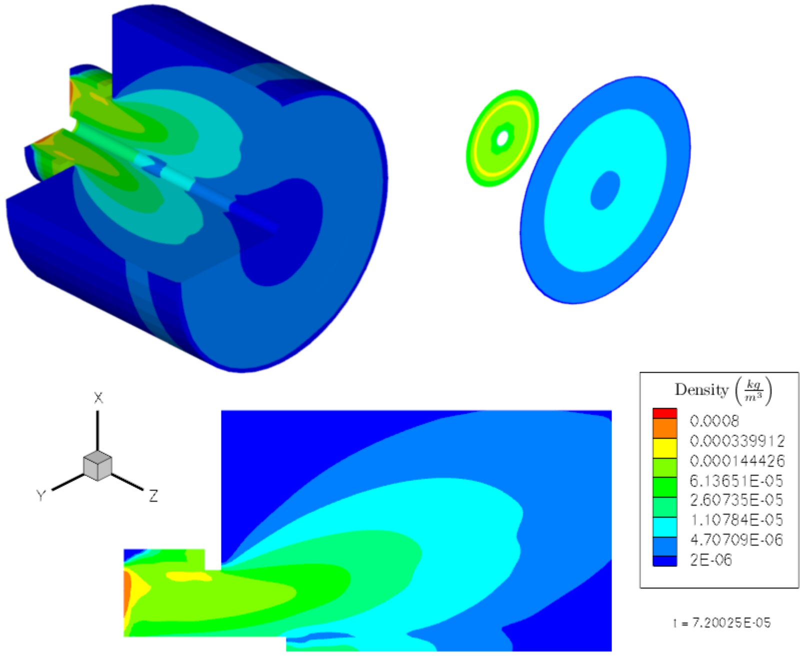

Figure 21. MACH3 density contours at $J = 24kA$ and $\dot{m} = 6g/s$

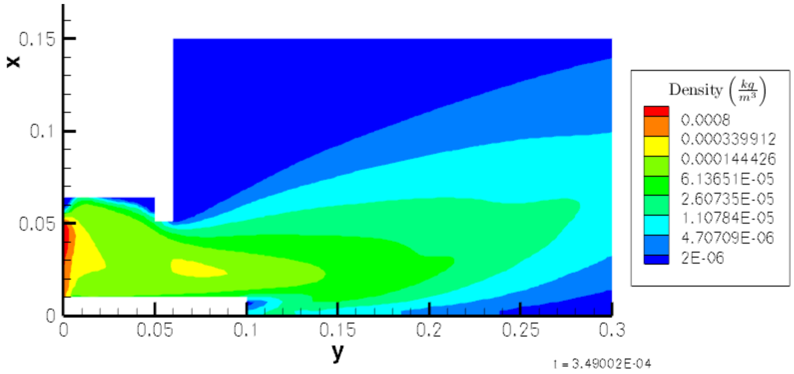

Figure 22. MACH2 density contours at $J = 24kA$ and $\dot{m} = 6g/s$

density contours expanding into the plume. Additionally, the differences due to dissimilar boundary conditions become much less pronounced with the increase of mass-flow rate. The $J = 24kA$ at $\dot{m} = 6g/s$ case, shown in figures 21 and 22, show similar distributions with the stronger applied current causing the difference to become more evident.

MACH3 and MACH2 predict very similar temperature distributions as well, except for the inconsequential anode-exhaust interface region, the differences of which arise from the different boundary conditions previously mentioned. For the region that contains the bulk of the mass for the $J = 12kA$ at $\dot{m} = 1g/s$ case, (see Figures 23 and 24), MACH predicts an average temperature range of $1.5eV < T < 2.5eV$. As the mass-flow rate is increased to $\dot{m} = 6g/s$, (see Figures 25 and 26), the temperature decreases, as expected, to an average range of $0.5eV < T < 1.5eV$. Similarly, when the power input is increased by increasing the operating current to $J = 24kA$, (see Figures 27 and 28), the average temperature range is $1eV < T < 2eV$. In all cases we note that elevated temperature ranges are produced, which in turn implies that thrust performance can benefit from solid-wall nozzle expansion allowing additional conversion of propellant enthalpy to exhaust kinetic energy. The elevated temperature values computed in the plume regions close and extending along the centerline and in the otuer edges of the plume region are a consequence of the lower densities computed in such regions. In these regions the

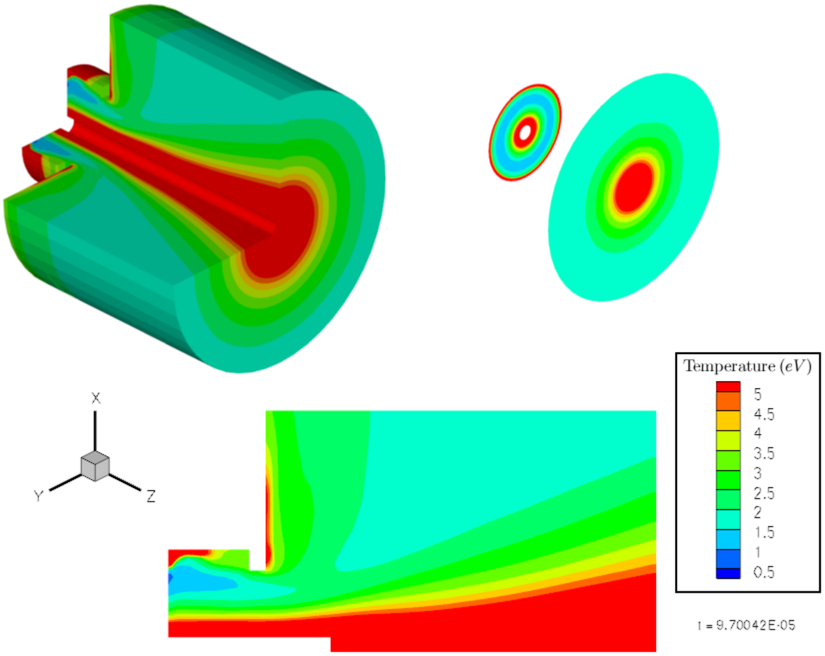

Figure 23. MACH3 temperature contours at $J = 12kA$ and $\dot{m} = 1g/s$

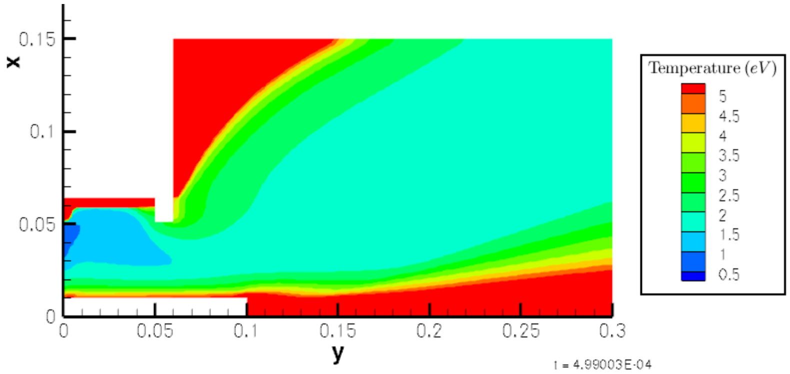

Figure 24. MACH2 temperature contours at $J = 12kA$ and $\dot{m} = 1g/s$

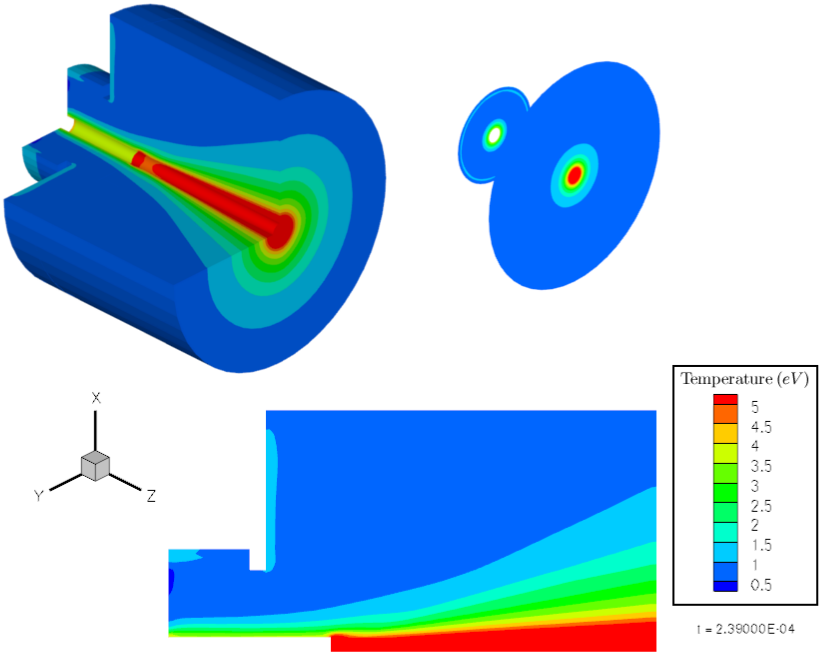

Figure 25. MACH3 temperature contours at $J = 12kA$ and $\dot{m} = 6g/s$

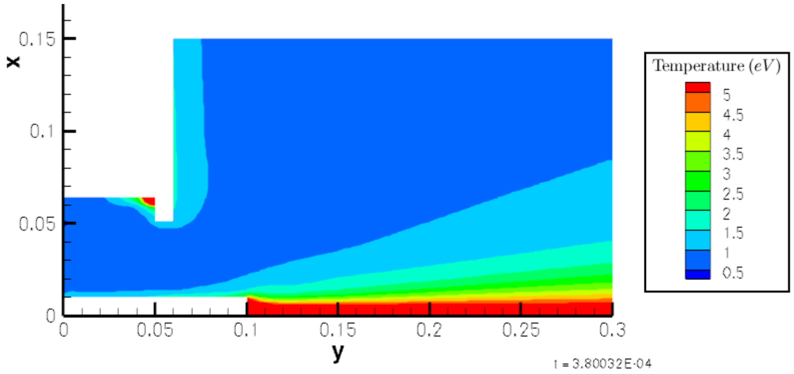

Figure 26. MACH2 temperature contours at $J = 12kA$ and $\dot{m} = 6g/s$

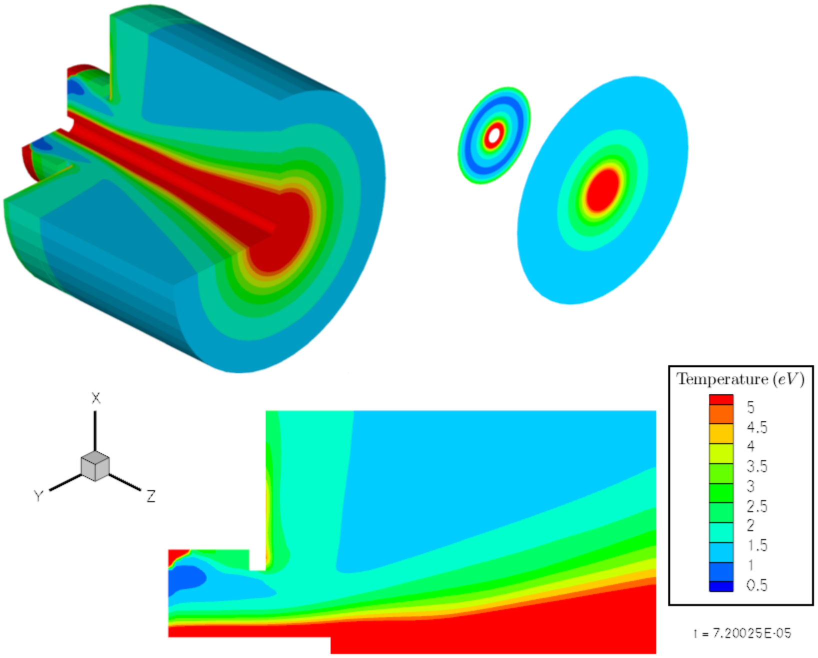

Figure 27. MACH3 temperature contours at $J = 24kA$ and $\dot{m} = 6g/s$

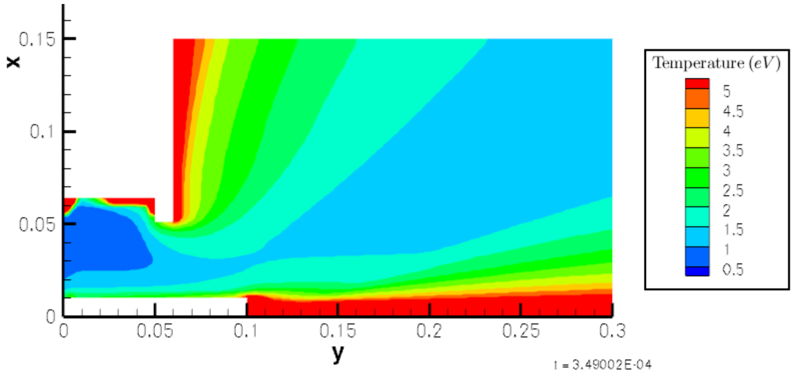

Figure 28. MACH2 temperature contours at $J = 24kA$ and $\dot{m} = 6g/s$

justification of the continuum assumption is challenged. Such very low density regions, however, negligibly contribute to the overall integrated performance characteristics of the rocket.

The plots of current distribution, in figures 29-34, also follow expected trends. It is clearly evident that the choice of the extended plume region is adequate to include the total current, which indicates that the total available current distribution is included in the calculation of the electromagnetic component of the computed thrust. For both versions of the code, the anode attachment is affected by the boundary condition, but the distributions show very little current attachment to the cathode in any case, with less than an eighth of the cathode attached at the most. The minimal current cathode attachment supports the choice of $\delta = 0$ for the Maecker thrust formula previously used to produce the best comparison with experimental thrust.

Figures 35 and 36 show distributions of the average ionization level (ζ) for $\dot{m} = 1g/s$ and $J = 12kA$ from MACH3 and MACH2. Because of the low mass-flow rate, the propellant is fully ionized very close to the backplate. The distributions are, aside from the dissimilar boundary condition, similar in magnitude and layout. The highest ionization rates occurr near the electrodes and in the centerline, which corresponds to regions with highest temperature, or greatest energy deposition to interal modes. Much like the temperature distributions, however, these regions contain the lowest densities and thus

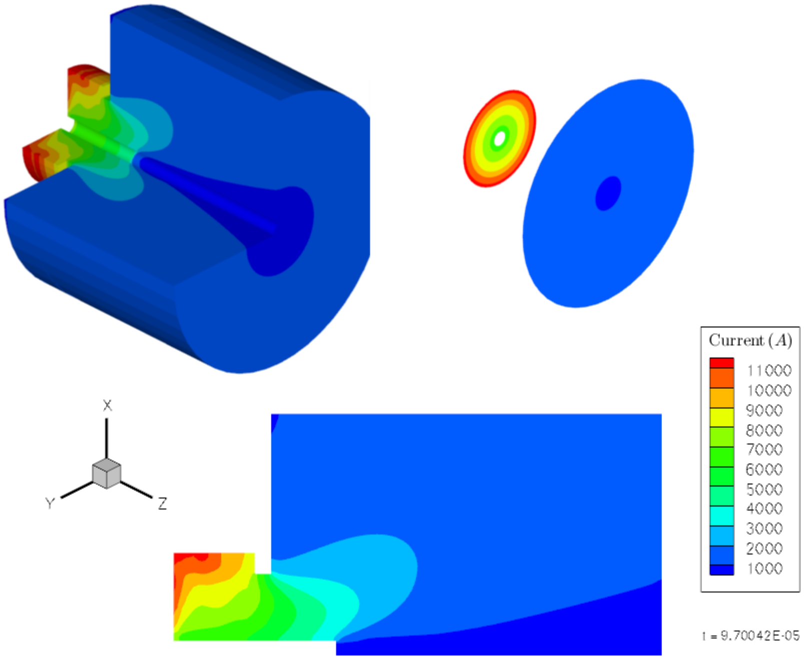

Figure 29. MACH3 currents contours at $J = 12kA$ and $\dot{m} = 1g/s$

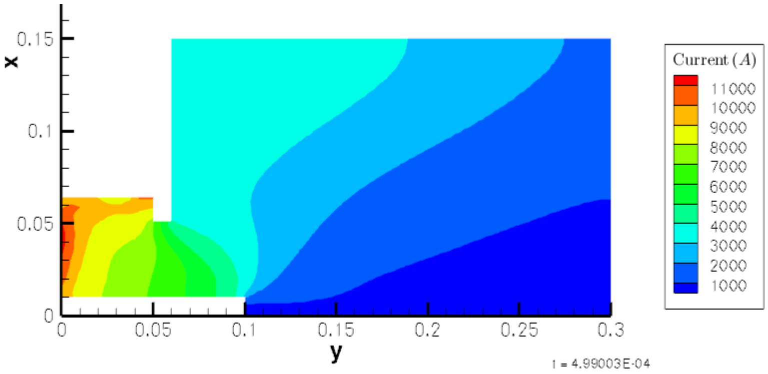

Figure 30. MACH2 currents contours at $J = 12kA$ and $\dot{m} = 1g/s$

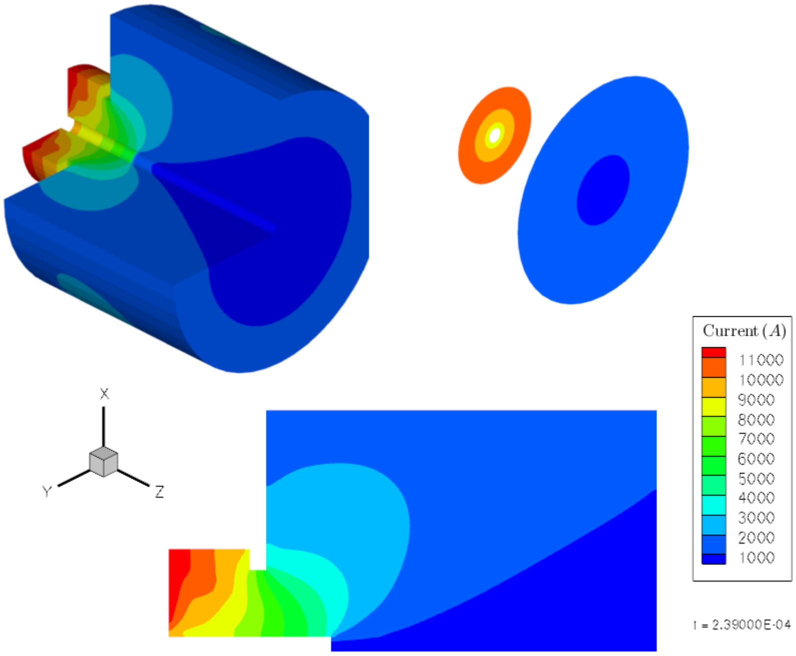

Figure 31. MACH3 currents contours at $J = 12kA$ and $\dot{m} = 6g/s$

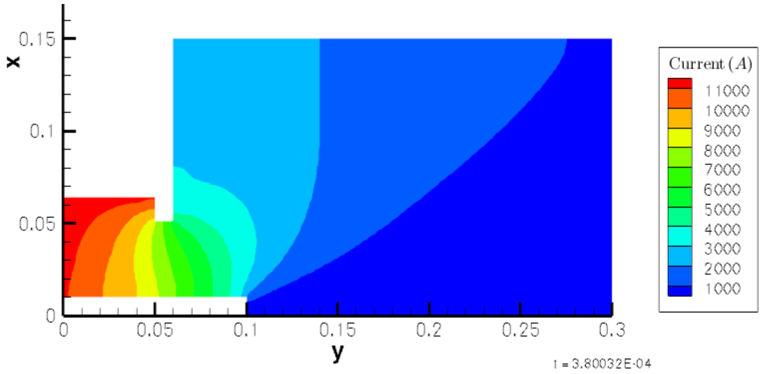

Figure 32. MACH2 currents contours at $J = 12kA$ and $\dot{m} = 6g/s$

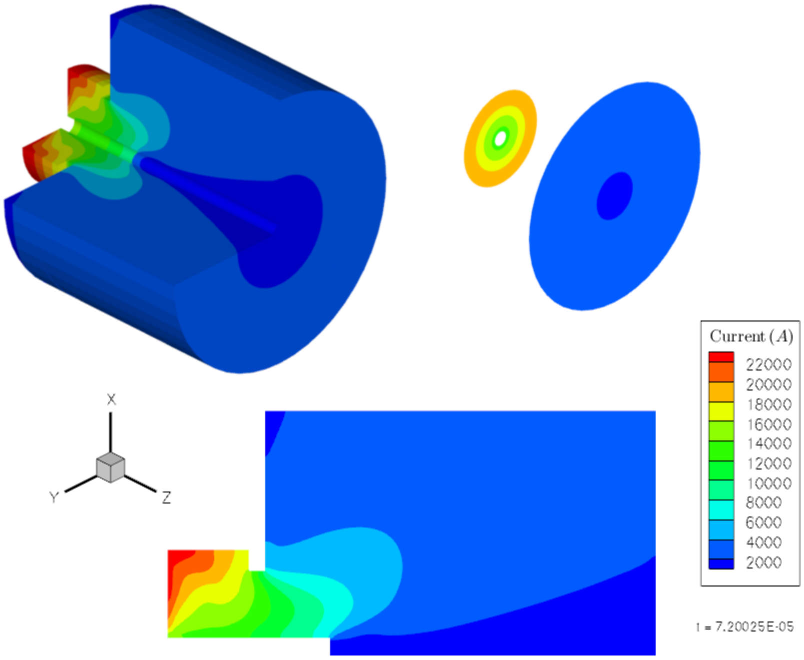

Figure 33. MACH3 current contours at $J = 24kA$ and $\dot{m} = 6g/s$

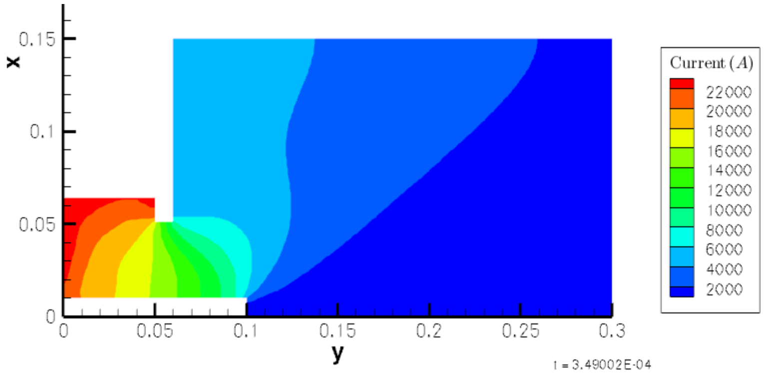

Figure 34. MACH2 current contours at $J = 24kA$ and $\dot{m} = 6g/s$

negligibly contribute to the overall integrated performance characteristics. The bulk of the mass in the simulation, in both versions of the code, is at an ionization level of about $\zeta \sim 2$.

Figures 37 and 38 show plots for ζ at $\dot{m} = 6g/s$ and $J = 12kA$ from MACH3 and MACH2. Because the mass-flow rate is increased six-fold with no increase in current, the ionization levels are significantly decreased in comparison to the $\dot{m} = 1g/s$ case. From the plots, it is clear that the plasma doesn't even become fully ionized for this operating condition. We would expect that at this operating condition there would be an elevated thermal contribution to thrust due to conversion of enthalpy. This is also confirmed by Figure 9, where the measured and simulated thrust values are greater than the Maecker formula which only represents the electromagnetic component.

Figures 39 and 40 show plots for ζ at $\dot{m} = 6g/s$ and $J = 24kA$ from MACH3 and MACH2. The ionization levels aren't as high as for the $\dot{m} = 1g/s$ and $J = 12kA$ case, but the plasma is fully ionized within the thrust chamber and the bulk of the mass reaches an ionization level in the range $1 < \zeta < 1.5$.

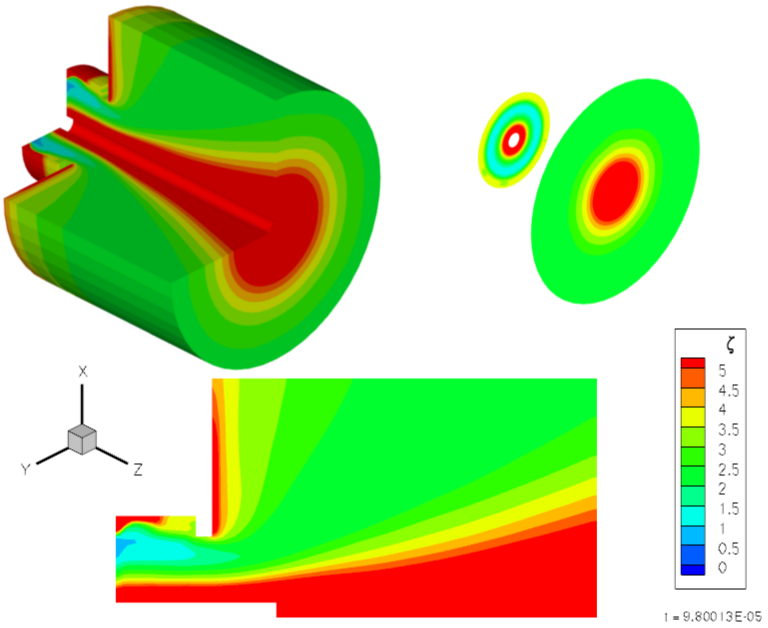

Figure 35. MACH3 average ionization level contours at $J = 12kA$ and $\dot{m} = 1g/s$

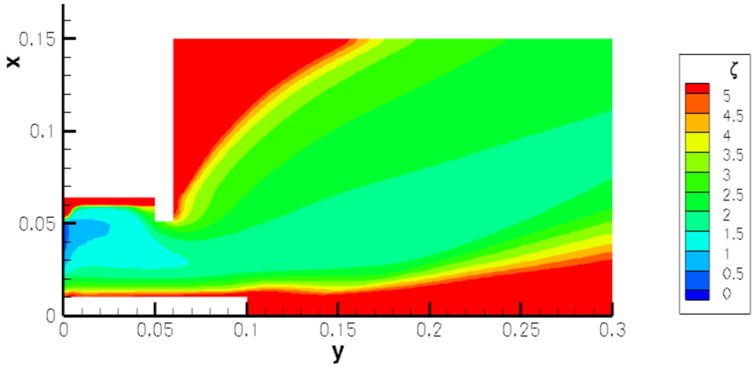

Figure 36. MACH2 average ionization level contours at $J = 12kA$ and $\dot{m} = 1sg/s$

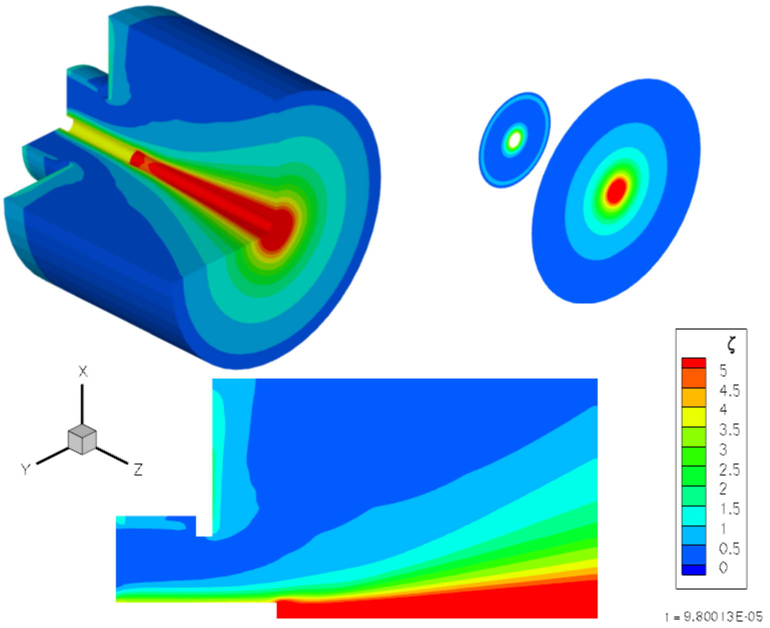

Figure 37. MACH3 average ionization level (ζ) contours at $J = 12kA$ and $\dot{m} = 6g/s$

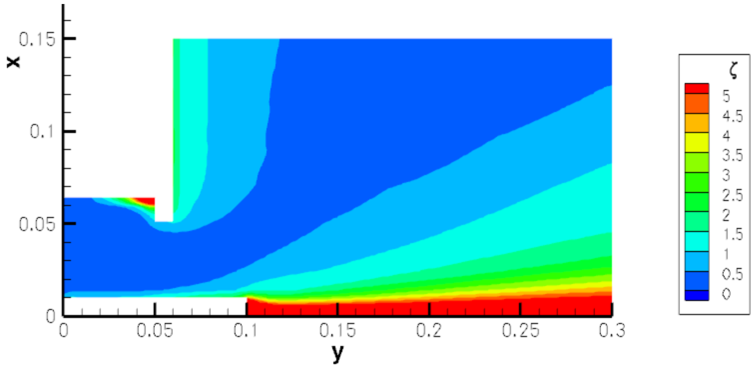

Figure 38. MACH2 average ionization level (ζ) contours at $J = 12kA$ and $\dot{m} = 6g/s$

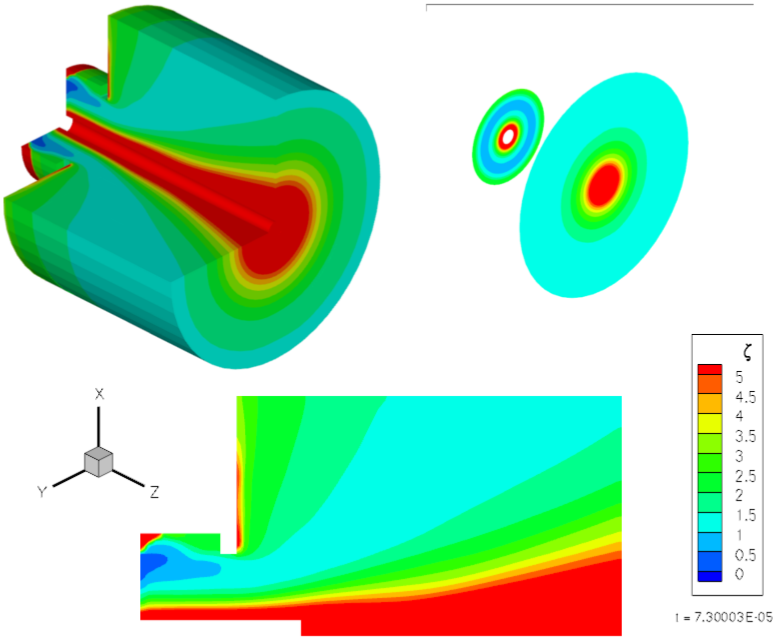

Figure 39. MACH3 average ionization level (ζ) contours at $J = 24kA$ and $\dot{m} = 6g/s$

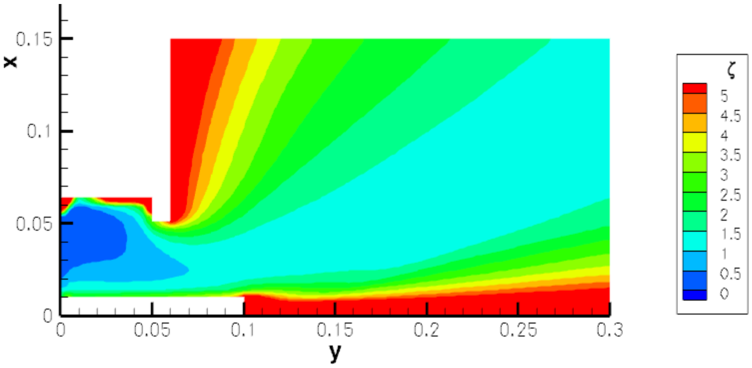

Figure 40. MACH2 average ionization level (ζ) contours at $J = 24kA$ and $\dot{m} = 6sg/s$

CHAPTER 7

CONCLUSION

The motivation for this study was to develop a model capable of addressing the inherently three-dimensional plasma flow of a self-field magnetoplasmadynamic (MPD) thruster. Even though the flow produced by the rocket operating at $\frac{J^2}{\dot{m}}$ values below the onset criterion has been shown to be reasonably captured within the two-dimensional axisymmetric assumption, operation beyond onset has been experimentally confirmed as highly three-dimensional. Furthermore, three-dimensional modeling capability allows for exploration and design of non-axisymmetric propellant injection schemes which are the established methods for operating such rockets. The main focus of this study was to develop, verify (by comparisons to the well-established two-dimensional axisymmetric version of the same model), and validate (by comparisons to experimental data) a fully three-dimensional model of steady-state magnetoplasmadynamic (MPD) thruster operation. This incorporated the following developments: 1) Modify the three-dimensional magnetohydrodynamic (MHD) code, MACH, so it can be utilized to model an MPD in steady-state operation. 2) Develop an accurate physical model of an MPD that can be simulated in MACH. 3) Use the developed model to generate predictions of the performance and flow characteristics of an MPD for a range of operating conditions. 4) Verify and validate the predicted performance and flow characteristics by comparisons to experimental data and by comparisons to identical simulations using the previously validated two-dimensional code, MACH2.

Fully three-dimensional simulations of an MPD thruster operating at steady-state were produced using the simulation code MACH3, described in more detail in section 4. MACH3 was upgraded to a 64-bit code in order to utilize the available computational resources of the Saguaro Cluster at Arizona State University, described in section 5.3. Additionally, the code was upgraded to compute performance characteristics of interest to rocket scientists. These included the integration over the exhaust boundary conditions to calculate thrust and mass-flow rate, and the intergatrion of induced currents in the thrust chamber to calculate plasma voltage. Thrust and plasma voltage were the primary performance characteristics used for verification.

Once upgraded, MACH3 was used to simulate the Princeton Benchmark Thruster (PBT) with the following operating conditions: $\dot{m} = 1g/s$ between $6.5kA < J < 12.7kA$, $\dot{m} = 3g/s$ between $10.6kA < J < 20.9kA$, and $\dot{m} = 6g/s$ between $10.9kA < J < 23.25kA$. This thruster and operating conditions were chosen for verification because of the ample availablility of experimental data[38].

Agreement to experimentally measured thrust for lower to medium-level current operation was also shown to be well within empirical uncertainty for mass-flow operation within $1g/s < \dot{m} < 6g/s$. A more substantial discrepancy (up to $\sim 20\%$) between experiment and simulation was observed at current operation beyond such values at which “onset” related phenomenon are present in experiment, e.g. significant voltage fluctuations. This implies that perhaps certain physical processes that may be associated with such fluctuations are modeled by neither MACH2 nor MACH3; the latter indicating that such phenomenon may not be inherently three dimensional and related to the plasma—as suggested by other efforts—but rather a consequence of electrode material processes which have not been incorporated into the current models.

Validation of the newly developed three-dimensional MHD code, MACH3, has been partially accomplished by thrust comparisons to experimental data and the well-established, repeatedly validated two-dimensional, axisymmetric version of the code, MACH2. Specifically, the predicted thrust values from the two numerical models are in excellent agreement, indicating that MACH3 can be expected to be as predictive as MACH2 has demonstrated over multiple applications to MPD thrusters.

Plasma Voltage-Current characteristics were also produced by the simulations. Comparisons of calculated plasma voltage to experimental total voltage serves as an estimate of the fall voltages maintained within thin sheaths in the vicinity of the electrodes to sustain a voltage drop across a mainly neutrally-charged plasma propellant. Such estimates are determined by the difference between plasma and total voltage. In turn, such computation allows for the estimation of power deposited to the sheaths; these comparisons showed that the majority of the input power ($\sim 60\%$ to $\sim 80\%$) is deposited into the electrode sheaths instead of the propellant, thus substantially degrading thrust efficiency.

In addition, the simulated plasma voltages do not contain the expected non-linearity and voltage hash present in the experimental total voltage at operating conditions exhibiting the symptoms of the onset phenomenon. These comparisons support the hypothesis that these effects are primarily associated with an electrode, material-related phenomenon such as anode spotting[8, 27], which coincides with the breakdown of azimuthal symmetry. Anode spotting involves 'hot spots', or spots where the flow of current between the electrodes concentrates instead of distributing uniformly and may be initiated by electrode material imperfections and roughness. These spots of high current, and resulting high temperature, deteriorate the electrode, causing pits and ablation of extra mass into the thrust chamber. The current model using MACH does not include the possibility for such surface variations, even though it is within its capability since the three-dimensional version can combine azimuthal boundary variation coupled with several ablation models already included in MACH. Instead, the electrodes are simply region boundaries with specified uniform, ideal boundary conditions. As a result, no fluctuations in mass-flow rate or voltage hash can be predicted.

In order to further confidence in the predictive capability of the newly developed three-dimensional version of the MACH code, the two-dimensional version was utilized to simulate the same operating conditions for relevant comparisons. MACH3 and MACH2 show excellent agreement, which gives confidence in MACH3's ability to model MPDs as MACH2 has already been verified in several previous efforts[9, 7, 8]. The performance characteristics of MACH2 and MACH3 agree to within $\sim 5\%$. The flowfield distributions also correlate very well even at different grid densities. The only disparity between the two code flowfield predictions emerges from imposing different boundary conditions in a region far downstream of the thruster's exit, and it was shown inconsequential to the overall magnitudes of performance characteristics calculated. The three-dimensional simulations can also be used to examine the nature of the flow-field in the azimuthal direction, which MACH2 assumes is axisymmetric. For the simulations performed, though, the azimuthal distributions show symmetry, even in the range of operating conditions where the MPD thruster is subject to symptoms associated with onset. In order to be consistent with what experimental observations show, a breakdown in azimuthal symmetry is expected in this range. Since MACH3 does not show such azimuthal asymmetry it can be concluded that processes associated with onset may be a consequence of material-dependent properties and imperfections of the electrode surfaces as opposed to plasma induced instabilities of thermochemical adjustment of the propellant in order to adjust the lower density operation.

7.1. Future Work

This study has shown that MACH3 is a robust simulation code that can be effectively used to predict and examine MPD thruster operation. As MACH2 was used to gain invaluable insights into performance limitations of MPD operation, the three-dimensional nature of MACH3 may lead to even greater understanding of MPD performance, including the onset phenomenon. This study was focused on verifying a simple model of the PBT thruster against available experimental data, but the three-dimensional nature of the code makes it promising for many possibile applications. To help understand the axisymmetric nature of the flow with respect to mass injection, the geometry can be modified to implement a more realistic mass injection scheme. This will increase the complexity of the geometry, and it may be necessary to upgrade the code to improve the passing of boundary information between processors.

Most importantly, however, such MACH3 simulations can be extended to study and further confirm that onset phenomenon are initiated by electrode-dependent processes as opposed to plasma related processes. This—which is well within the present capabilities of the code—can be accomplished by modeling azimuthally asymmetric electrode boundary conditions with the capability of ablation and geometry variations. In this manner, we can closely model "spot" processes which have been observed as small regions of high current concentration and electrode mass injection.

APPENDIX A

BOUNDARY CONDITION FIX

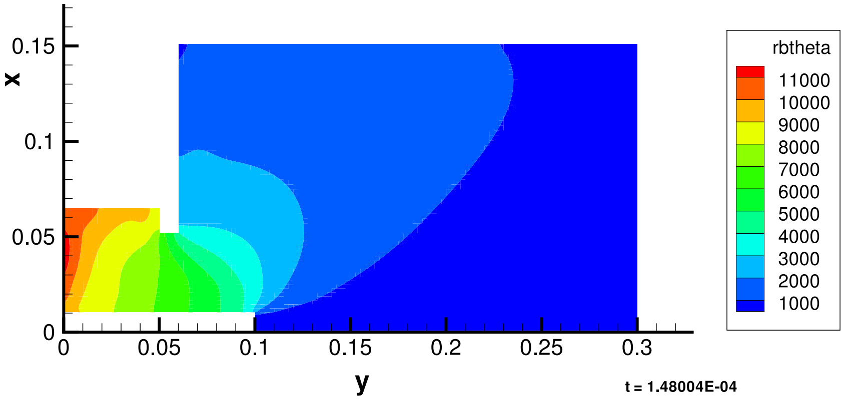

Figure 41. MACH2 current contours at $J = 12kA$ and $\dot{m} = 1sg/s$ with vacuum boundary conditions

REFERENCES

[1] R. G. Jahn, *Physics of Electric Propulsion.* McGraw-Hill, 1968.

[2] M. R. LaPointe, "High power mpd thruster performance measurements," in *40rd AIAA/ASME/SAE/ASEE Joint Propulsion Conference & Exhibit*, (Ft. Lauderdale, Florida), July 2004.

[3] J. L. Lawless and V. V. Subramaniam, "Theory of onset in magnetoplasmadynamic thrusters," *Journal of Propulsion and Power*, vol. 3, pp. 121–127, 1987.

[4] V. V. Subramaniam and J. L. Lawless, "Onset in magnetoplasmadynamic thrusters with finite-rate ionization," *Journal of Propulsion and Power*, vol. 4, pp. 526–532, 1988.

[5] J. C. Preble, "Onset in magnetoplasmadynamic thrusters: A model of an electrothermal instability," Master's thesis, Massachusetts Institute of Technology, 1990.

[6] F. Paganucciand, M. Zuinand, M. Agostiniand, M. Andrenucciand, V. Antoni, M. Bagatinand, F. Bonomoand, R. Cavazzanaand, P. Franzand, L. Marreli, P. M. E. Martinesand, P. Rossettiand, G. Serianniand, P. Scarin, M. Signoriand, and G. Spizzo, "Mhd instabilities in magneto-plasma-dynamic thrusters," *Plasma Physics and Controlled Fusion*, vol. 50, 2008.

[7] P. G. Mikellides, "Modeling and analysis of a megawatt-class magnetoplasmadynamic thruster," *Journal of Propulsion and Power*, vol. 20, pp. 204–209, 2004.

[8] P. G. Mikellides, *A Theoretical Investigation of Magnetoplasmadynamic Thrusters.* PhD thesis, Ohio State University, Columbus, OH, December 1994.

[9] P. G. Mikellides, P. J. Turchi, and N. F. Roderick, "Applied-field magnetoplasmadynamic thrusters, part 1: Numerical simulations using the mach2 code," *Journal of Propulsion and Power*, vol. 16, pp. 887–893, 2000.

[10] P. G. Mikellides and P. J. Turchi, “Applied-field magnetoplasmadynamic thrusters, part 2: Analytic expressions for thrust and voltage,” *Journal of Propulsion and Power*, vol. 16, pp. 894–901, 2000.

[11] B. Parma and P. G. Mikellides, “Modeling of magnetoplasmadynamic, (mpd) acceleration in three dimensions,” in *43rd AIAA/ASME/SAE/ASEE Joint Propulsion Conference & Exhibit*, (Cincinnati, OH), July 2007.

[12] K. Sankaran, S. C. Jardin, and E. Y. Choueiri, “Comparison of simulated plasma flowfields to experimental measurements for a gas-fed magnetoplasmadynamic thruster,” in *39rd AIAA/ASME/SAE/ASEE Joint Propulsion Conference & Exhibit*, (Huntsville, AL), July 2003.

[13] N. Nerheim and A. Kelly, “A critical review of the magnetoplasmadynamic thruster for space applications,” *NASA CR-92139*, 1968.

[14] J. Sovey and M. Mantenieks, “Performance and lifetime assessment of magnetoplasmadynamic arc thruster technology,” *Journal of Propulsion and Power*, vol. 7, pp. 71–83, 1991.

[15] R. Myers, M. Mantenieks, and M. LaPointe, “Mpd thruster technology,” in *Magnetoplasmadynamic Thruster Workshop*, (NASA Lewis Research Center), 1991.

[16] K. Sankaran and E. Y. Choueiri, “An accurate characteristics-splitting scheme for numerical solution of mhd equations,” in *26th International Electric Propulsion Conference*, (Kitakyushu, Japan), 1999.

[17] K. Sankaran, L. Martinelli, S. C. Jardin, and E. Y. Choueiri, “A flux-limited numerical method for solving the mhd equations to simulate propulsive plasma flows,” *International Journal For Numerical Methods in Engineering*, vol. 53, pp. 1415–1432, 2002.

[18] K. Sankaran, E. Y. Choueiri, and S. C. Jardin, “Application of a new numerical solver to the simulation of mpd flows,” in *36rd AIAA/ASME/SAE/ASEE Joint Propulsion Conference & Exhibit*, (Huntsville, AL), July 2000.

[19] J. Heiermann and M. Auweter-Kurtz, "Numerical and experimental investigation of the current distribution in self-field magnetoplasmadynamic thrusters," *Journal of Propulsion and Power*, vol. 21, pp. 119–128, 2005.

[20] I. K. K. Toki and M. Tanaka, "Current distribution on the electrodes of mpd arcjets," *AIAA Journal*, vol. 20, pp. 889–892, 1982.

[21] T. Ao and T. Fujiwara, "Numerical and experimental study of an mpd thruster.," in *17th International Electric Propulsion Conference*, (Tokyo, Japan), pp. 55–64, 1984.

[22] T. Miyasaka and T. Fujiwara, "Numerical prediction of onset phenomenon in a 2-dimensional axisymmetric mpd thruster.," *AIAA Paper 99-2432*, 1999.

[23] E. Y. Choueiri, "Anomalous resistivity and heating in current-driven plasma thrusters.," *Physics of Plasmas*, vol. 6, 1999.

[24] H. J. Kaeppeler, C. Boie, M. Auweter-Kurtz, and P. C. Sleziona, "Application of adaptive numerical schemes for mpd thruster simulation.," in *25th International Electric Propulsion Conference*, (Cleveland, OH), 1997.

[25] J. Heiermann, M. Auweter-Kurtz, J. J. Kaeppeler, A. Eberle, U. Iben, , and P. C. Sleziona, "Recent improvements of numerical methods for the simulation of mpd thruster flow on adaptive meshes," in *26th International Electric Propulsion Conference*, (Kitakyushu, Japan), 1999.

[26] D. C. Lilekis and R. E. Peterkin, "Effects of azimuthal injection asymmetry of mpd thruster performance using the mach3 code," in *24th International Electric Propulsion Conference*, (Moscow, Russia), 1995.

[27] L. Uribarri and E. Y. Choueiri, "Creation of onset voltage hash by anode spots in a magnetoplasmadynamic thruster," *Journal of Propulsion and Power*, vol. 25, p. 949, 2009.

[28] E. Y. Choueiri, K. A. J., and R. G. Jahn, "Current-driven plasma acceleration versus current-driven energy dissipation, part ii: Electromagnetic wave stability theory and experiments," in *21th International Electric Propulsion Conference*, (Viareggio, Italy), October 1991.

[29] V. V. Subramaniam and J. L. Lawless, "The electrical characteristics of magnetoplasmadynamic thrusters," in *IEEE International Conference on Plasma Science*, 1985.

[30] P. J. Turchi, "Critical speed and voltage-current characteristics in self-field plasma thrusters," *Journal of Propulsion*, vol. 2, pp. 398–401, 1986.

[31] D. Q. King, K. E. Clark, and R. G. Jahn, "Effect of choked flow on terminal characteristics of mpd thrusters," in *15th International Electric Propulsion Conference*, (Las Vegas, Nevada), April 1981.

[32] E. Y. Choueiri, "Scaling of thrust in self-field magnetoplasmadynamic thrusters," *Journal of Propulsion and Power*, vol. 14, pp. 744–753, 1998.

[33] F. F. Chen, *Introduction to Plasma Physics and Controlled Fusion*, vol. 1. Plenum Press, 1984.

[34] R. E. Peterkin, M. H. Frese, and C. R. Sovinec, "Transport of magnetic flux in an arbitrary coordinate ale code," *Journal of Computational Physics*, vol. 140, pp. 148–171, 1998.

[35] R. E. Peterkin and M. H. Frese, *MACH2: A Reference Manual - First Edition.* U.S. Air Force Research Laboratory, 3550 Aberdeen Ave SE, Kirtland AFB, NM 87117-5776, September 1998.

[36] M. H. Frese, "Mach2: A two-dimensional magnetohydrodynamic simulation code for complex experimental configurations," in *Mission Research Corp.*, (Albuquerque, NM), 1987.

[37] D. Allison, "An ammonia thermochemical model for the study of pulsed inductive thruster processes," Master's thesis, Arizona State University, 2004.

[38] E. Y. Choueiri and J. K. Ziemer, “Quasi-steady magnetoplasmadynamic thruster performance database,” in *34th AIAA, SAE, ASME, and ASEE, Joint Propulsion Conference and Exhibit*, (Cleveland, OH), July 1998.

[39] R. Burton, K. Clark, and R. Jahn, “Measured performance of a multimegawatt mpd thruster.,” *Journal of Spacecraft and Rockets*, vol. 20, pp. 299–304, 1983.

[40] E. Y. Choueiri and H. Okuda, “Anomalous ionization in the mpd thruster,” in *23th International Electric Propulsion Conference*, (Seattle, WA), 1993.

[41] J. Gilland and G. Johnston, “Mpd thruster performance analytic models,” *Expanding the Frontiers of Space*, vol. 654, pp. 516–524, 2003.